Gondwana Research 133 (2024) 129–147

Contents lists available at ScienceDirect

Gondwana Research

journal homepage: www.elsevier.com/locate/gr

Discovery of Late Carboniferous high-grade carbonate-hosted manganese mineralization in the Maerkansu area of the Western Kunlun Orogen, Northwest China

Yongbao Gao [a], Leon Bagas [a], Yuegao Liu [b,*], Wenyuan Li [c,d], Keiko Hattori [e], Dominic Papineau [b,f], Delong Jing [d], Denghui Chen [d], Jiaxin Teng [d], Yongkang He [d], Min Zhao [d], Long Zhang [a], Zhe Zhao [g]

[a] Technology Innovation Center for Gold Ore Exploration, Xi'an Center of Mineral Resources Survey, China Geological Survey, Xi'an 710100, China
[b] Institute of Deep-sea Science and Engineering, Chinese Academy of Sciences, Sanya 572000, China
[c] School of Earth Sciences and Resources, Chang'an University, Xi'an 710054, China
[d] Key Laboratory for the Study of Focused Magmatism and Giant Ore Deposits, MNR, Xi'an Center of China Geological Survey, Xi'an 710054, China
[e] Department of Earth Sciences, University of Ottawa, Ottawa K1N 6N5, Canada
[f] Department of Earth Sciences, London Centre for Nanotechnology, and Centre for Planetary Sciences, University College London, London WC1H 0AH, UK
[g] Command Center of Natural Resource Comprehensive Survey, China Geological Survey, Beijing 100032, China

ARTICLE INFO

Article history:
Received 25 September 2023
Revised 8 June 2024
Accepted 8 June 2024
Available online 13 June 2024
Handling Editor: Jan Marten Huizenga

Keywords:
Western Kunlun Orogen
Tarim mantle plume
Rhodochrosite
Paleo-Tethys Ocean
Microbial mediation

ABSTRACT

The Aoertuokanashi deposit located in the Western Kunlun Orogen is the first known Late Carboniferous large high-grade carbonate-hosted Mn deposit in the world and it has been mined since 2018. The deposit is considered to have formed in a back-arc basin developed during the northward subduction of the Paleo-Tethys Ocean beneath the Tarim Block. The Re-Os isotope isochron age of Mn ore at the Aoertuokanashi deposit is 302 ± 9 Ma. The minimum initial $^{187}Os/^{188}Os$ values obtained from the deposit is 0.28, which indicates the presence of a mantle source for the mineralization. The Aoertuokanashi deposit is similar in age to the 301 ± 5 Ma Wajilitag kimberlite in the Tarim Block, which is considered to be the initial magmatic pulse triggered by the Tarim mantle plume. The Late Carboniferous Aoertuokanashi Mn deposit was likely promoted by igneous activity from the Tarim mantle plume.

The Aoertuokanashi deposit shows geochemical characteristics of hot water activity in a back-arc basin. The Mn mineralization is hosted in the restricted platform facies. Framboidal pyrite, typical biomat, and authigenic quartz are observed in the Mn deposit, indicating the influence of microbial processes. The sedimentary facies show a starving basin feature that can enhance microbial mediation. The $\delta^{13}C_{V\text{-}PDB}$ values of mineralized rocks (from −19.5 to −8.2 ‰) are more negative than those of wall rocks (from −5.3 to + 4.2 ‰), whereas the $\delta^{13}C_{V\text{-}PDB}$ values (around −29 ‰) of kerogen for the Mn ore are significantly lower than those of the whole rock. These compositions indicate that the reducing function of organic matter played an important role in Mn mineralization. In the inferred extensional tectonic environment, under the influence of a mantle plume, the stratum with strong hot water activities and a large amount of organic matter becomes the focal point for the formation of carbonate type manganese ore deposit.

© 2024 The Author(s). Published by Elsevier B.V. on behalf of International Association for Gondwana Research. This is an open access article under the CC BY license (http://creativecommons.org/licenses/by/4.0/).

1. Introduction

Manganese is a strategically critical metal. Most Mn deposits in China are in southwest and western parts and they are small- (<2 Mt Mn) to medium-sized (2–20 Mt Mn), with only 12 large deposits with reserves > 20 Mt of Mn (Jiang et al., 2016; Yu et al., 2016; Zhou et al., 2016; Xiao et al., 2017; Chen et al., 2019; Ma et al., 2019; Li et al., 2018; Zhang et al., 2020; Li et al., 2022b). High-grade (>25 wt% Mn) Mn-carbonate deposits have been recently discovered in the Western Kunlun Orogen (WKO), such as the large Aoertuokanashi and Muhu deposits, and the medium-size Malkantu deposit in the Maerkansu Mn belt, which is the first known Late Carboniferous belt in the world containing high-grade (>25 wt% Mn) Mn-carbonate mineralization. Mineralization in these deposits is stratiform with average grades of >35 wt% and they extend ~100 km long trending west towards Tajikistan, which represents the richest Mn-carbonate ore field in China (Gao et al., 2017). By the end of 2017, total Mn resource of the belt was estimated to be >45 Mt (Gao et al., 2018).

* Corresponding author.
E-mail address: liuyg@idsse.ac.cn (Y. Liu).

https://doi.org/10.1016/j.gr.2024.06.006
1342-937X/© 2024 The Author(s). Published by Elsevier B.V. on behalf of International Association for Gondwana Research.
This is an open access article under the CC BY license (http://creativecommons.org/licenses/by/4.0/).

In the global perspective, the Carboniferous is not known for major Mn mineralization (Kuleshov, 2011; Schier et al., 2020). The Late Carboniferous Mn mineralization in the WKO is therefore unusual, possibly linked to a special tectonic environment. The Paleo-Tethys Ocean existed between the Tarim Craton and the Gondwana continent during the Late Carboniferous (Han et al., 2016; Ding et al., 2017; Dong et al., 2022). Manganese deposits have been found in some terranes around the Paleo-Tethys Ocean, such as the Late Devonian Xialei Mn deposit (360 Ma) in South China (Chen et al., 2023), the Late Devonian Kawame Fe-Mn deposit (368 Ma) in Northeast Japan (Kuwahara et al., 2022), and the Early Triassic Dongping Mn deposit (250 Ma) in South China (Chen et al., 2023). However, in the Paleo-Tethys Ocean tectonic domain, Late Carboniferous large-scale Mn deposits have only been found in the WKO, where the Paleo-Tethys Ocean subducted northward. There was no Mn mineralization during the same period when the Paleo-Tethys Ocean subducted northward beneath the North China Block and the Qaidam Block. This leads to the following question: what was the tectonic environment in the WKO that led to Mn mineralization?

Manganese is an element commonly used by microorganisms, and some famous high-grade Mn deposits are closely related to microbial mediation (Polgári et al., 2016; Wang et al., 2018; Yao et al., 2018). Whether a Mn deposit has undergone microbial mediation needs comprehensive support from mineral features, organic matter composition, whole-rock geochemistry, and isotope data (Polgári and Gyollai, 2022). According to the occurrences of framboidal pyrite in carbonaceous argillaceous limestone and its sulfur isotopes, some researchers have suggested that microbial mediation happened in the Aoertuokanashi deposit (Zhang et al., 2020). However, there has been no other report from the Late Carboniferous Mn deposits in the WKO that indicates microbial mediation, for instance from the observation of silicate minerals, organic matter composition, and the oxygen fugacity. This limits the understanding of this high-grade large Mn ore deposit with a unique metallogenic age.

To enhance the understanding of the Late Carboniferous high-grade Mn-carbonate mineralization, we have selected the Aoertuokanashi Mn deposit in the WKO for a detailed study including sedimentary facies analysis, observation of typical microbial mediation silicate mineral and rock structure, Re-Os and U-Pb dating, organic geochemistry, and S and C isotope analysis.

2. Regional geology

The Late Paleozoic Maerkansu Mn belt is located in western China at the junction of a back-arc basin of North WKO and the Tarim Block (Fig. 1a, b). The Mn belt includes the large Aoertuokanashi and Muhu deposits, and the medium-sized Maerkantu deposit (Fig. 1c). The WKO is located between the Tarim Basin to the north and the Tianhuihai-North Qiangtang Terrane to the south (Fig. 1a, b). It can be divided into two tectonic units: the North WKO and the South WKO. North WKO and South WKO are separated by the early Paleozoic ophiolite-bearing Kudi-Qimanyute suture zone, which is considered a relic of the Proto-Tethys Ocean (Pan, 1990; Xiao et al., 2005; Zhang et al., 2019), but this suture zone is not apparent in the study area. South WKO is a magmatic arc developed on Precambrian basement. The magmatic rocks consist mainly of Early Paleozoic magmatism and a small part of Late Paleozoic-Mesozoic magmatism, which represent the subduction process of the Proto-Tethys Ocean and the Paleo-Tethys Ocean, respectively (Pan, 1990; Mattern and Schneider, 2000; Xiao et al., 2002; Wang et al., 2020). The North WKO consists of a Precambrian basement covered by Devonian red molasse and Carboniferous-Permian shallow marine carbonate rocks, which is considered an uplifted part of the Tarim Block (Li et al., 2011).

The study area includes the Tarim Basin to the north, North WKO, and the Tianshuihai-North Qiangtang Belt to the south, which are separated by the Wuchibielishankou-Akecheyi and Kongbeili-Muzhaling faults (Fig. 1b, c). The Wuchibielishankou-Akecheyi Fault (known as the Kegang Fault to the east, Fig. 1b and c) is a lithospheric fault that existed during the Early Carboniferous (She et al., 2020; Zhang et al., 2022). The Kongbeili-Muzhaling Fault is the westward extension of the Kangxiwa Fault (suture zone) (Fig. 1b, c), which represents the location of the termination of the Paleo-Tethys Ocean (Mattern and Schneider, 2000; Li et al., 2011).

The units exposed in the North WKO in the study area include Devonian-Permian successions and Quaternary sediments (Fig. 1c). The Devonian succession is composed of sandstone, shale, and limestone. The Carboniferous rocks consist of the Early Carboniferous Wuluate Formation and the Late Carboniferous Kalaatehe Formation. The Wuluate Formation is exposed in the eastern part of the Mn belt and includes volcanogenic massive sulfide deposits such as the Aketashi and Saluoyi deposits. The Wuluate Formation includes pillow basalt, andesite, and a small amount of rhyolite with minor limestone and feldspathic greywacke, which is speculated to be formed in the shallow sea environment in the center of the North WKO back-arc basin (Yun et al., 2015). The Late Carboniferous Kalaatehe Formation consists of limestone and sandstone. The limestone hosts Mn-rich layers (Fig. 1c). The contact between the Wuluate Formation and the Kalaatehe Formation is planar and conformable, whereas the Carboniferous units are unconformably overlain by Permian rocks. The Early Permian succession is composed of altered andesite, rhyolitic tuff and monzogranitic porphyry. These igneous rocks occur along SE-trending faults.

3. Geological characteristics of the deposit

3.1. Geology of the Aoertuokanashi Mn deposit

The Aoertuokanashi deposit occurs in the western portion of the Maerkansu Mn belt (Fig. 1c). The exposed rocks belong to the Late Carboniferous Kalaatehe, Early Permian Maerkanquekusaishan, Late Cretaceous Kukebai, and Late Cretaceous Jiangejieer formations (Fig. 2). The Kalaatehe Formation hosts the Mn mineralization and is subdivided into a lower member consisting of bioclastic calcirudite, a middle member consisting of carbonaceous argillaceous limestone hosting the Mn mineralization, and an upper member consisting of micrite. The Late Permian Maerkanquekusaishan Formation is subdivided into a lower member consisting of marble, purplish-red feldspar sandstone, and some grey to green sandstone, and an upper member consisting of grey to green altered andesite and minor amounts of tuff with brecciated crystals. The Early Permian Maerkanquekusaishan Formation is unconformably overlain by the Late Cretaceous Kukebai Formation and is composed of lime-green sandstone, siltstone, mudstone, and purplish feldspathic sandstone. The formation is >300 m in thickness (Figs. 2 and 3).

The Aoertuokanashi Mn ore layers are situated in an anticline (Fig. 2). The core of the anticline is in the southern part of the mining area and trends eastward, and comprises Carboniferous rocks. The northern limb of the anticline dips between 69° and 82° to the north, and the southern limb dips ~ 72° to the south (Fig. 2). The Mn mineralization is located on the northern limb where the Kalaatehe Formation is exposed (Fig. 2). Minor Late Permian altered andesite is exposed in the northern limb of the anticline (Fig. 2). A normal fault in the north of the mining area is the bound-

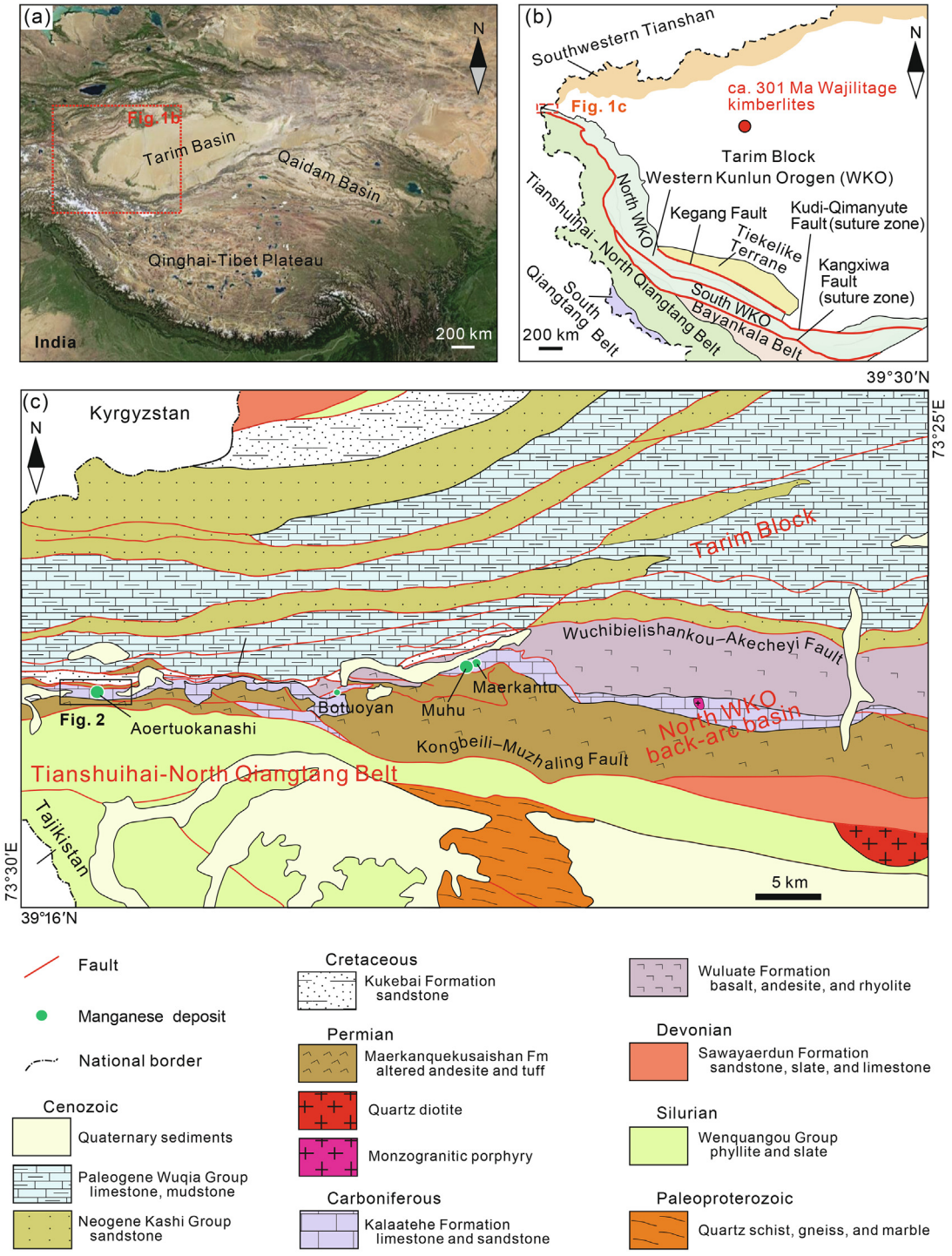

Fig. 1. Maps showing: a) the study area (image from Google Maps; b) tectonic sketch map of Western Xinjiang in Western China, and the age of the Wajilitage kimberlite intrusion (Zhang et al., 2013); c) regional geological map and location of Mn deposits in the Maerkansu area of the Western Kunlun Orogen, Western China (modified after Gao et al., 2018).

ary between the andesite layer and the Kalaatehe Formation (Fig. 2), which dips ~ 54° to the north. There is a reverse fault in the south of the mining area, which is the boundary between the Late Permian tuff and the Kalaatehe Formation.

3.2. Characteristics of the lower and upper members of the Kalaatehe Formation

The Mn mineralization is situated in Kalaatehe Formation, which extends in an eastward direction and comprises a 395 m thick lower member, 165 m thick middle member, and 86 m thick upper member (Figs. 3 and 4). Mn ore layers (Mn grade > 15 wt%) exist in the middle member.

The lower member consists of thick grey to black, medium- to coarse-grained, layered bioclastic calcirudite, calcarenite, and thick beds of calcirudite, with a thin interlayer of fine-grained limestone. About 10 % of the calcirudite contains fragments of ostracods, foraminifera, and gastropods, and ~80 % of the unit contains fragments of volcanic rocks (Fig. 5a), including andesite and dacite, and 10 % detrital quartz and feldspar. The above lithology indicates

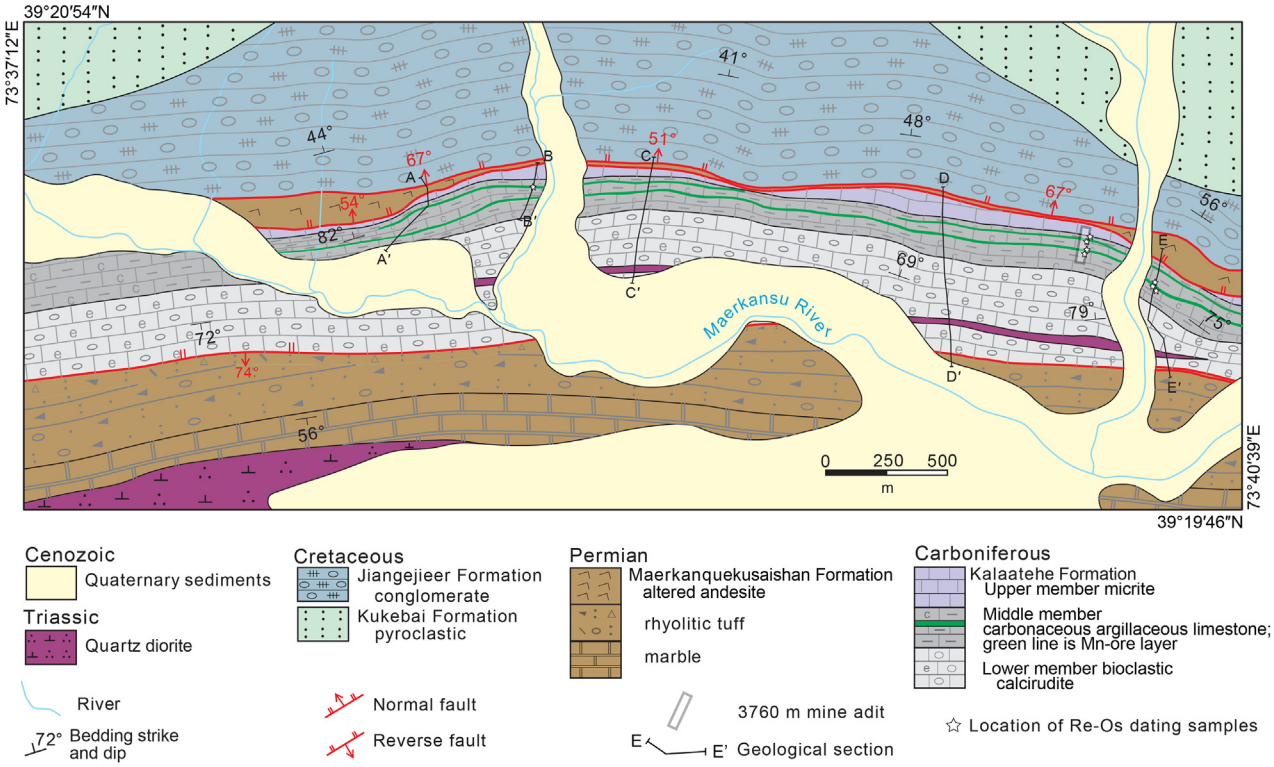

Fig. 2. Geological map of the Aoertuokanashi Mn deposit, Western Kunlun Orogen (modified after Gao et al., 2018).

a platform shoal facies as the depositional paleoenvironment (Fig. 4).

The upper member consists of grey to black, medium- to thickly bedded micrite interbedded with calcarenite (Fig. 5b) and crystalline limestone. The rocks are characterized by shallow-water organisms such as bivalves and gastropods. The rocks of the upper member are consistent with the open platform facies (Fig. 4), in an oxygenated environment under the wave base.

3.3. Characteristics of the middle member of the Kalaatehe Formation

The middle member of the Kalaatehe Formation hosts the manganese ore beds and is subdivided into lower and upper units. The lower unit includes interbedded light grey thin-layered pyrite-bearing carbonaceous argillaceous limestone, cyclic interbedded medium- to thick-bedded calcarenite (Fig. 5c), and thin-bedded layered silty limestone. The calcarenite contains subrounded quartz grains, suggesting a distal source or active water movement during deposition. Herringbone cross-bedding structures are observed in calcarenite, indicating the lower part of the middle member is tidal flat facies.

The upper unit is dominated by pyrite-bearing carbonaceous argillaceous limestone, with light-grey and thinly layered calcarenite, light-grey thinly layered silty limestone containing algae debris, and Mn-rich bioclastic limestone (Fig. 5d–f). The rocks are characterized by a high organic content, up to 1.7 wt%. The carbonaceous argillaceous limestone with horizontal bedding is dark and contains pyrite-rich laminae, suggesting deposition in deep-water reduced environments with a slow sedimentation rate. This unit belongs to restricted platform facies, the most important Mn-bearing facies.

The calcarenite in the middle member is composed of 80–90 % calcite grains, 5–10 % plagioclase, 5–10 % quartz, and < 5 % andesitic and dacitic fragments. The sand-size grains (0.1–0.35 mm) are angular to sub-rounded.

The calcarenite is conformably overlain by carbonaceous argillaceous limestone containing > 50 vol% fossils, such as crinoids, cephalopods, and ostracods (Fig. 5d-f). The carbonaceous argillaceous limestone contains authigenic quartz grains that are 0.1–0.2 mm in diameter (Supplementary Fig. 1). It commonly hosts two Mn-rich horizons that are ~ 50 m apart. The Mn-rich horizons are composed of ~ 90 % rhodochrosite with biological debris (Fig. 5e). The rhodochrosite (0.03–0.25 mm) is subhedral to anhedral in crystal habit. Some of the Mn ores have a primary laminar layering (Fig. 5e).

The two Mn-rich horizons at the Aoertuokanashi deposit are locally referred to as the No. I and No. II orebodies. The No. I horizon extends continuously for ~ 5500 m in an eastward direction and dips steeply (~80°) towards the north (Fig. 2). The orebody is on the northern limb of the Aoertuokanashi anticline where its thickness ranges from 0.4 to 22 m, with an average thickness of ~ 4 m and an average grade of 35 wt% Mn.

The No. II horizon is ~ 50 m north of the No. I horizon (Fig. 2). The No. II horizon can be followed for ~ 2500 m, and dips ~ 80° to the north. The horizon is 0.6–8.4 m thick averaging 2 m and has an average grade of 29 wt% Mn.

3.4. Ore and mineral combination characteristics

The ore rocks consist of 80 % rhodochrosite with minor manganocalcite (or manganoan calcite), sussexite, and sulfides (Fig. 5g–j). Based on the observations and analyses with polarising microscopy, electron probe micro-analyser, and scanning electron microscopy, the Mn-carbonate is laminated and consists of clay-size particles. There are mainly two metallogenic periods in the mining area, the sedimentary diagenetic period and the hydrothermal reformation period. Minerals in the sedimentary diagenetic

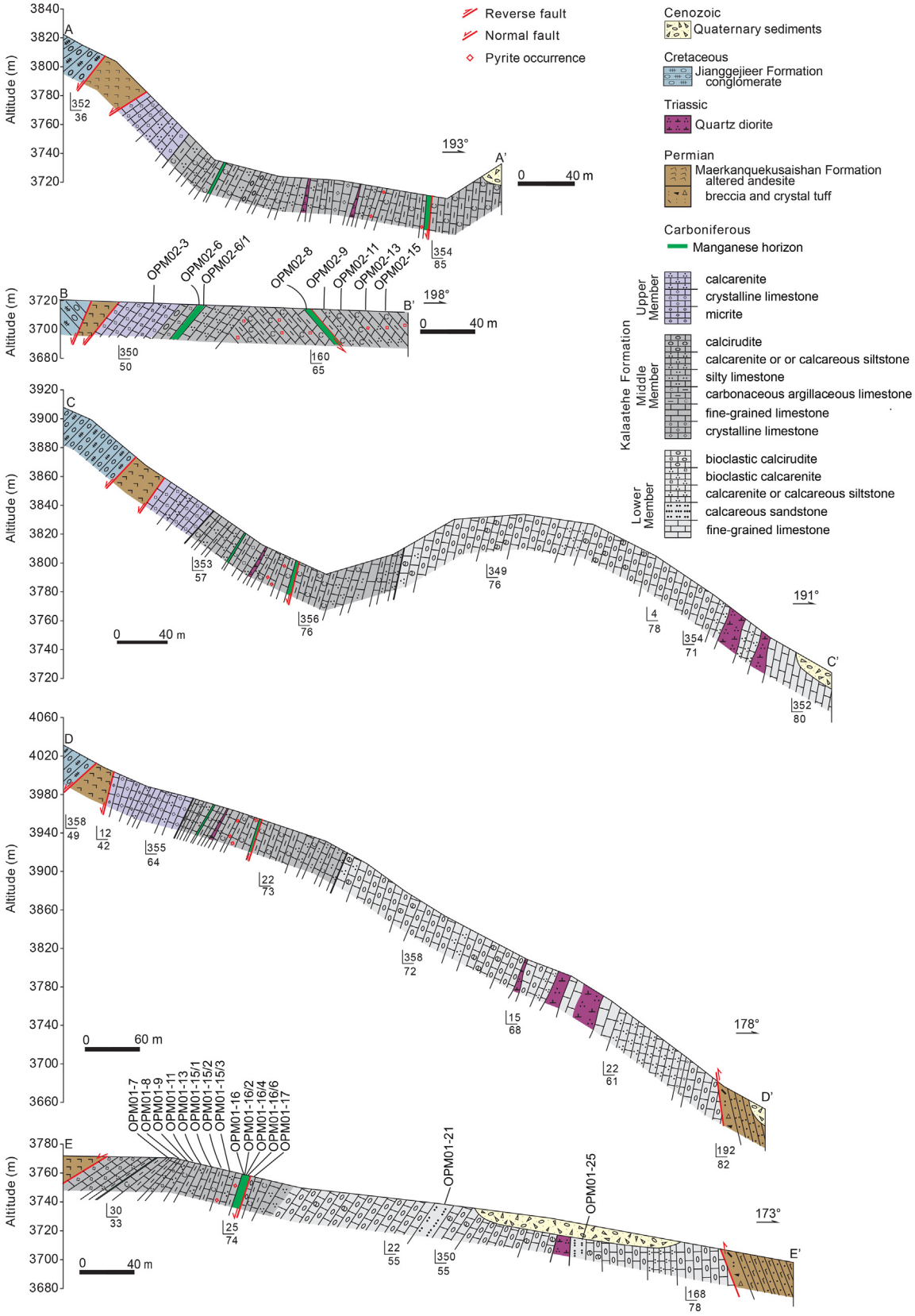

Fig. 3. Representative geological profiles of the Aoertuokanashi Mn deposit showing the sampling numbers and locations.

period mainly include rhodochrosite, manganocalcite, sussexite, and bementite. The rhodochrosite is black to brown and is cemented by manganocalcite and argillite. The rhodochrosite is coeval with manganocalcite, disseminated sulphides, and sussexite (Fig. 5g–j). The particle size of the rhodochrosite is 2–30 μm in diameter. The volume fraction of sulfide is less than 0.5 %, which

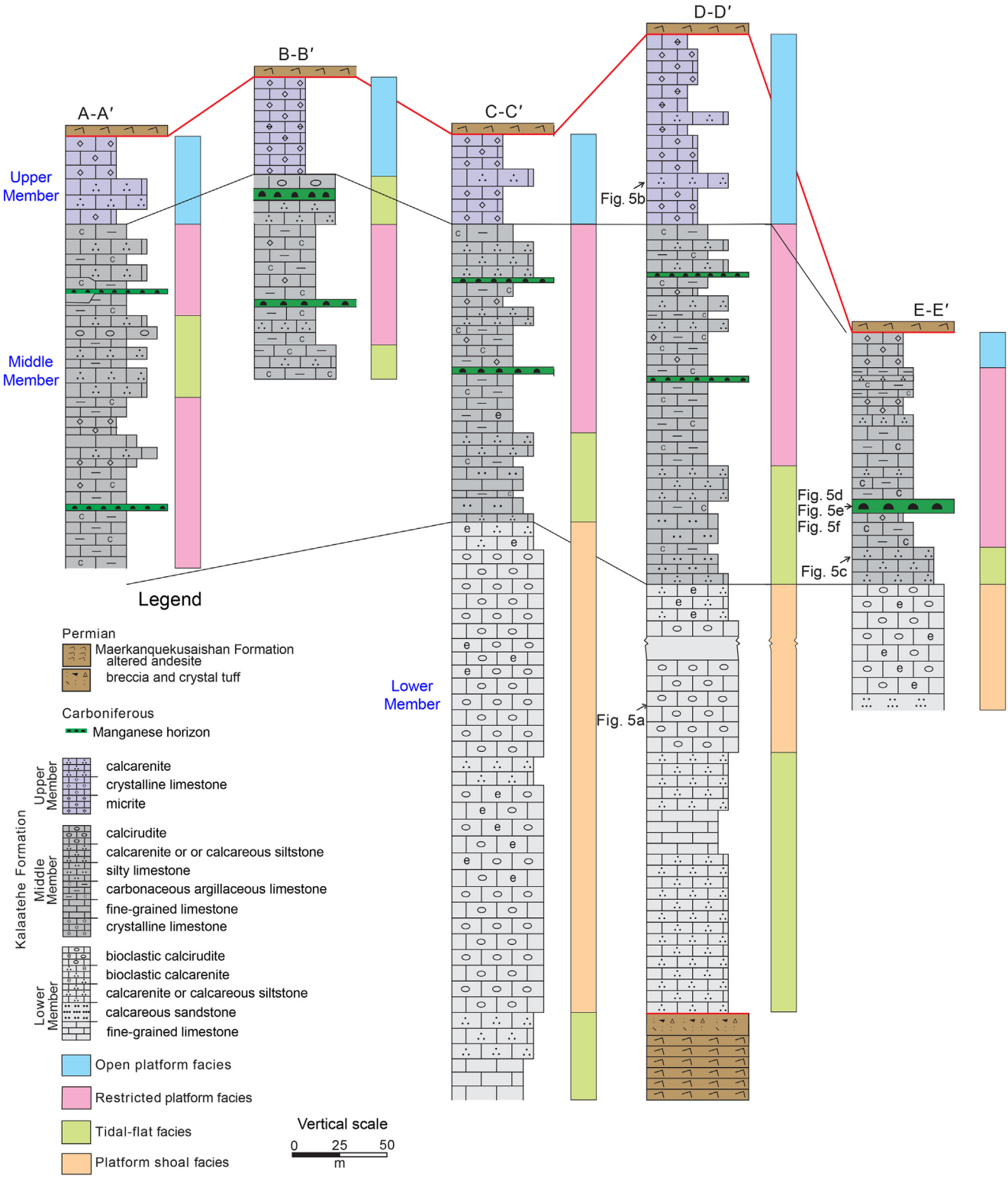

Fig. 4. Lithofacies comparison and sedimentary facies of the Aoertuokanashi Mn deposit.

is composed mainly of euhedral cubic pyrite and a small amount of pyrrhotite (Fig. 5g–i). Occasionally framboidal pyrite occurs, but it does not form typical rosettes (Fig. 5h). Minerals in the hydrothermal reformation period consist of gypsum, manganocalcite, and manganchlorite. In this period, gypsum vein (Fig. 5k) or manganocalcite and manganchlorite vein (Fig. 5l) cut through the rhodochrosite.

4. Sampling

Eight Mn ore samples for Re-Os dating were collected from the Aoertuokanashi Mn mineralization, including four samples exposed in the mine adit at an elevation of 3760 m, three samples from geological section E, and one sample from geological section B (Fig. 2).

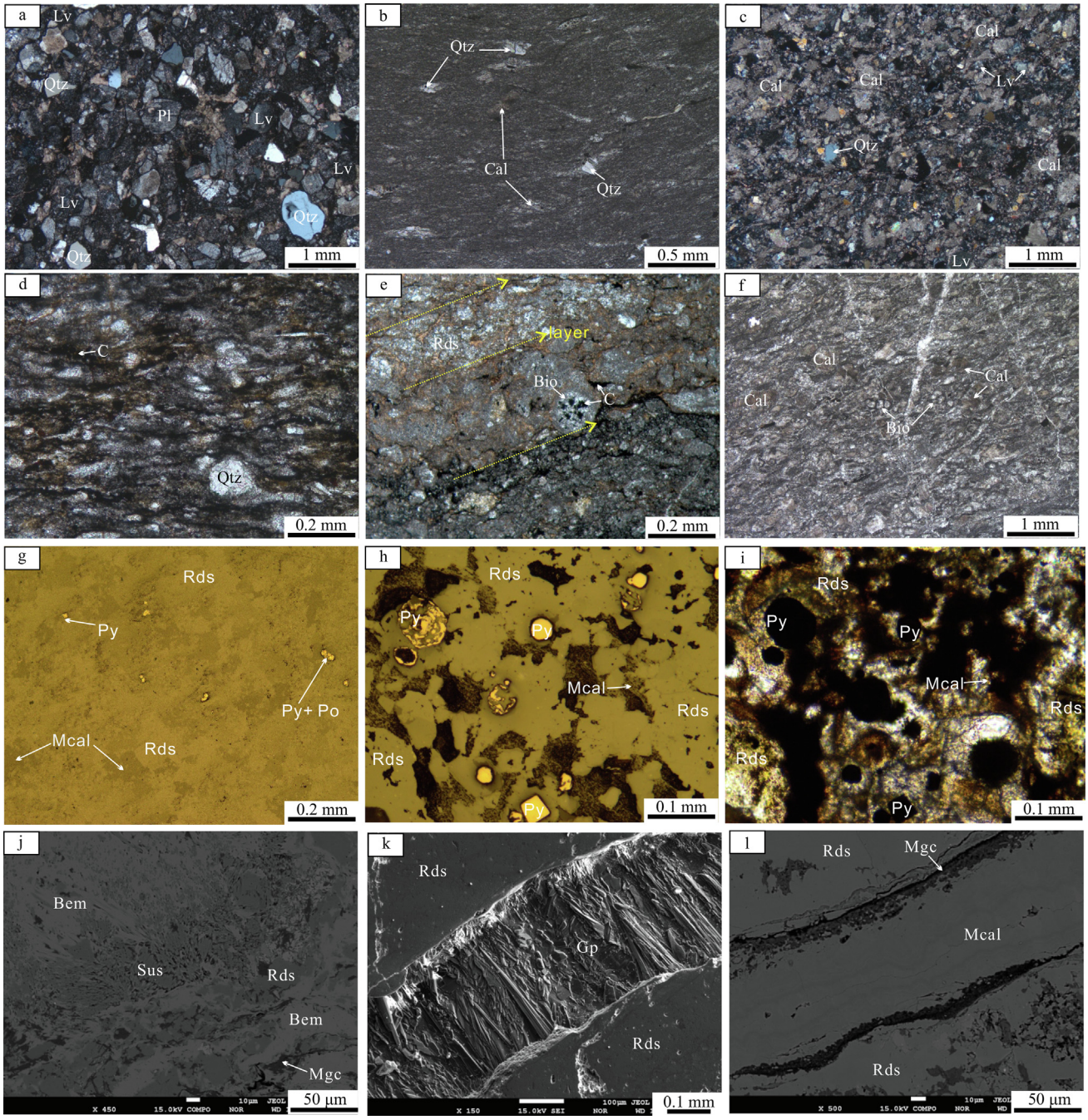

Fig. 5. Microscopic characteristics of typical rocks and ore: a) calcirudite from the lower member of the Kalaatehe Formation, with clasts of andesite and dacite, plagioclase, and quartz (cross-polarized light, XPL); b) calcarenite from the upper member of the Kalaatehe Formation (XPL); c) calcarenite in the middle member of the Kalaatehe Formation showing detrital calcite and plagioclase (XPL); d) carbonaceous argillaceous limestone in the middle member of the Kalaatehe Formation consisting of argillaceous components (XPL); e) manganese ore from the middle member of the Kalaatehe Formation, which is composed of rhodochrosite and bioclastic material (XPL); f) Carbonaceous bioclastic argillaceous limestone containing fine-grained detrial calcite and a small amount of crinoids (XPL); g) coeval rhodochrosite, manganocalcite and disseminated pyrite and pyrrhotite (under reflected-light); h) coeval rhodochrosite, manganocalcite, disseminated cubic pyrite, and framboidal pyrite (reflected-light); i) same area with Fig. 5h (under transmitted light); j) coeval rhodochrosite and sussexite (secondary electron image, SEI); k) gypsum cuts throught rhodochrosite (SEI); and l) manganocalcite and manganchlorite cut through rhodochrosite (SEI). Abbreviations: C = carbon, Qtz = quartz, Cal = calcite, Pl = plagioclase, Lv = volcanic rock fragments, Bio = bioclasts, Gp = gypsum, Rds = rhodochrosite, Mcal = manganocalcite, Bem = bementite, Py = pyrite, Po = pyrrhotite, Sus = sussexite, and Mgc = manganchlorite.

Rhyolitic tuff was collected for zircon U-Pb dating from the Early Permian Maerkanquekusaishan Formation overlying the Mn-bearing beds on the western side of the Muhu mining area (Fig. 1c). The sample is composed of pyroclastic rocks, including ~ 35 % of lithic debris, ~55 % of crystals, and ~ 10 % of volcanic ash. The composition of the lithic debris is rhyolitic with a size between 0.1 x 0.2 mm and 0.5 x 0.6 mm. The crystals include angular and sub-angular quartz, plagioclase, and minor K-feldspar, with a size between 0.1 x 0.1 mm and 0.5 x 0.5 mm. The lithic debris and crystal debris are cemented by volcanic ash.

Twenty-three samples were collected from the Aoertuokenashi Mn deposit for other geochemical analysis (Fig. 3), including seven from the footwall of Mn ore layer, seven from Mn ore layer, and nine from the hanging wall of Mn ore layer.

5. Analytical methods

Details of the methods involved in the analyses of samples are described in Appendix 1, including the analysis of whole-rock compositions, C-isotope compositions, total organic carbon contents, *in-situ* S isotope of sulfides, cold-cathodoluminescence features of quartz, zircon U-Pb geochronology, the Re-Os isotopes composition of organic matter in Mn ore rocks, and the gas chromatography-mass spectroscopy (GC–MS) of saturated hydrocarbons.

6. Results

6.1. Whole rock geochemistry

The composition of the major and trace elements for manganese ores and host rocks are listed in Sup. Table 1. The geochemistry of the trace elements in the Mn mineralization and the hanging wall and footwall rocks are listed in Sup. Table S1. The V/(V + Ni) mass ratio of seven samples of manganese ore is 0.23–0.62 averaging 0.39. The V/(V + Ni) mass ratios of the surrounding rocks vary from 0.15 to 0.90, with a mean value of 0.59. The Co/Ni mass ratios of the manganese ore are 0.20–0.77, with an average of 0.42.

The total rare earth elements (∑REE) content of manganese ore samples ranges from 44 to 284 ppm, with a mean value of 151 ppm (Sup. Table S1). The values of δCe are between 0.94 and 3.25, and δEu are between 0.45 and 1.23. Most samples have positive Ce anomalies and weak Eu negative anomalies on the PAAS (Post-Archean Australian Shale) normalized REE diagram (Fig. 6). The ∑REE content of the rocks at the hanging wall and footwall is 25–101 ppm (averaging 51 ppm), which is significantly lower than that of the manganese ore. The hanging and footwall rocks have δCe values between 0.53 and 1.25 and δEu values between 0.55 and 1.86 (Fig. 6), but the Eu anomaly changes greatly (Fig. 6). On the PAAS-normalized REE plot, the Mn ore is enriched in light REEs, showing a slightly left-leaning or flat curve (Fig. 6). In contrast, the hanging and footwall rocks are relatively low in light REE, showing a right-leaning curve (Fig. 6).

6.2. Carbon isotope compositions

The carbon isotope compositions of bulk carbonate are listed in Table 1. The $\delta^{13}C_{V\text{-}PDB}$ (V-PDB = Vienna Peedee Belemnite) values of carbonate in the manganese ore are –8.2 to −19.5 ‰, and $\delta^{13}C_{V\text{-}PDB}$ values of carbonate in the rocks below and above the mineralization show predominantly a lower range of values between −5.3 and + 4.2 ‰.

6.3. Bulk composition of organic carbon

The TOC content of the samples and $\delta^{13}C_{V\text{-}PDB}$ values of kerogen are listed in Table 2. The TOC content of the four Mn ore samples ranges between 0.2 and 0.6 wt%, with a mean value of 0.5 wt%. The $\delta^{13}C_{V\text{-}PDB}$ value for kerogen is between −27.9 and −29.9 ‰, with an average of −29.1 ‰.

Table 1
Carbon and oxygen isotopes of bulk carbonate for ore and host-rocks from the Aoertuokanashi deposit.

Location	Sample No.	Rock type	$\delta^{13}C_{V\text{-}PDB}$ ‰	Reference
Hanging wall	OPM01-7	Carbonaceous argillaceous limestone	+2.0	This paper
	OPM01-8	Micrite	-1.2	
	OPM01-9	Calcareous siltstone	+2.1	
	OPM01-11	Carbonaceous argillaceous limestone	-3.1	
	OPM01-13	Calcareous siltstone	-5.1	
	OPM01-15/1	Carbonaceous argillaceous limestone	+1.4	
	OPM01-15/2	Carbonaceous argillaceous limestone	-1.8	
	OPM01-15/3	Calcareous siltstone	-2.9	
	OPM02-3	Micrite	+4.2	
Mn ore	OPM01-16	Grey-black Mn ore	-12.1	
	OPM01-16/2	Grey-black Mn ore	-17.9	
	OPM0-16/4	Grey-black Mn ore	-8.2	
	OPM01-16/6	Grey-black Mn ore	-11.3	
	OPM02-6	Grey-black Mn ore	-19.5	
	OPM02-6/1	Grey-black Mn ore	-18.9	
	OR3	Mn ores	-20.2	Gao et al. (2018)
	OR5		-13.2	
	OR6		-23.2	
	OR7		-23.3	
	OR8		-20.8	
	OR9		-21.6	
	OR10		-21.8	
	OR11		-17.9	
	OR16-1		-16.1	
	OR16-2		-15.1	
	OR16-3		-14.3	
	OR16-4		-13.5	
	OR17-1		-13.9	
	OR17-2		-12.8	
	OR17-3		-21.4	
	OR17-4		-21.1	
Footwall	OPM01-17	Calcirudite	-3.1	This paper
	OPM01-21	Calcareous fine sandstone	+1.5	
	OPM01-25	Calcareous medium sandstone	-4.8	
	OPM02-9	Calcareous siltstone	-0.3	
	OPM02-11	Carbonaceous argillaceous limestone	-3.2	
	OPM02-13	Calcareous siltstone	-5.3	
	OPM02-15	Carbonaceous argillaceous limestone	+1.0	

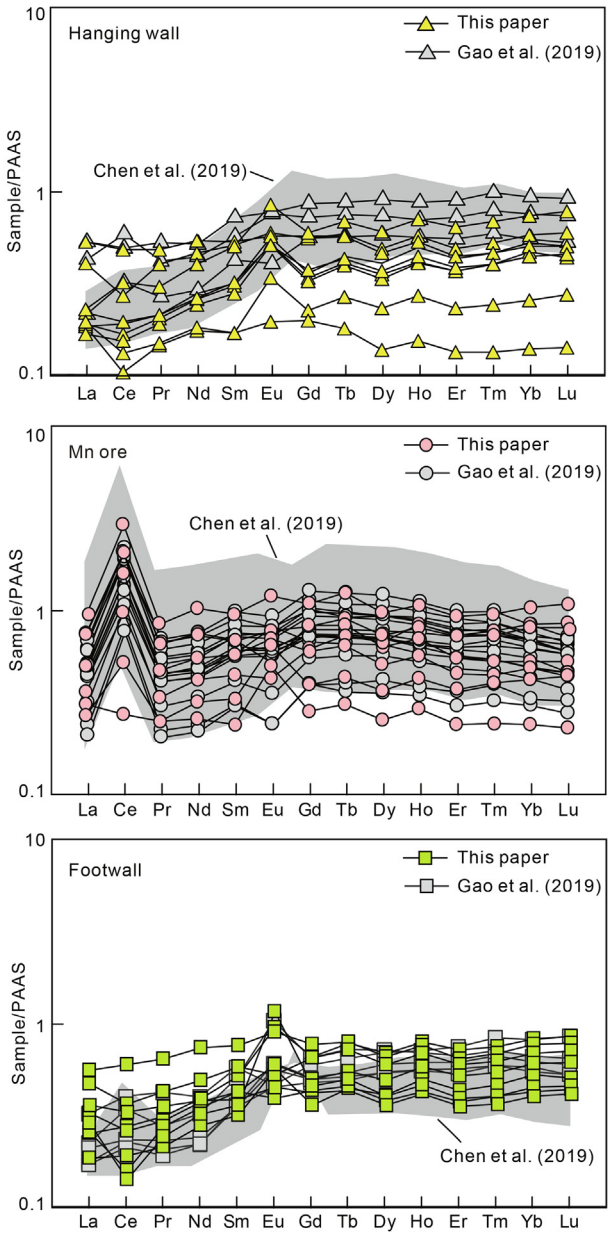

Fig. 6. Post Archean Australian Shale (PAAS)-normalized REE patterns for Mn ore and wall-rocks from the Aoertuokanashi Mn deposit. PAAS values are from McLennan (1989).

The footwall rocks have TOC contents between 0.5 and 1.6 % and kerogen $\delta^{13}C_{V\text{-}PDB}$ value from −28.5 to −29.1 ‰. The rocks in the hanging wall have TOC contents between 0.2 to 1.7 % and kerogen $\delta^{13}C_{V\text{-}PDB}$ values between −27.9 and −29.6 ‰.

6.4. Molecular composition of organic matter

The pristane/phytane (Pr/Ph) mass ratios of the footwall rocks, Mn ores, and hanging rocks are 0.29–0.63, 0.18–0.26, and 0.41–0.61, respectively (Table 2). The Pr/*n*-C_{17} mass ratios of the footwall rocks, Mn ores, and hanging rocks are 0.45–0.75, 0.41–0.59, and 0.62–2.69, respectively, and the Ph/*n*-C_{18} mass ratios of the footwall rocks, Mn ores, and hanging rocks are 0.29–0.63, 0.18–0.26, and 0.41–0.61, respectively (Table 2, Fig. 7a).

The *m*/*z* = 85 mass chromatogram of manganese ore shows that the main peak of *n*-alkanes is C_{24} (Fig. 7b), and there is no obvious difference in odd–even numbered masses. Among the terpanes (Fig. 7c), C_{23} tricyclic terpane (C_{23}TT) and C_{30} hopane (C_{30}H) are high in content; C_{19} tricyclic terpane was near the detection limit; while C_{24} tetracyclic terpane is low in content, and no biomarker contributed by higher plants such as orirane are found. Among the steranes (Fig. 7d), the C_{27}-C_{28}-C_{29} regular steranes show C_{27} sterane predominance and display in V-shape.

6.5. In-situ S isotopes

The *in-situ* sulfur isotope data of sulfides are listed in Table 3. The analysed sulfides include pyrrhotite, hypidiomorphic granular pyrite, and globular pyrite (Supplementary Fig. 2). The $\delta^{34}S_{v\text{-}CDT}$ values for pyrrhotite are between −8.4 and −5.6 ‰ (n = 4), hypidiomorphic granular pyrite are −7.9 to −3.5 ‰ (n = 8), and globular pyrite are −38.7 ‰ (n = 1).

6.6. Zircon u-pb geochronology

Over 500 zircon grains were extracted from rhyolitic tuff in the Early Permian Maerkanquekusaishan Formation overlying the manganese-bearing rocks. Twenty five transparent grains (40–200 μm) were selected for U-Pb isotopic dating. The zircon grains show an oscillating zoning in cathodoluminescent images without obvious inherited cores (Supplementary Fig. 3). The Th/U mass ratio of all these zircons range from 0.30 to 0.91 (Sup. Table S2).

Twenty five zircon grains of the rhyolitic tuff yielded Concordia ages between 282 and 309 Ma with a weighted average age of 292 ± 3 Ma (Fig. 8a). The age is considered to be the deposition age for the base of the Maerkanquekusaishan Formation.

Table 2
Organic carbon assay and isotopic data for the Aoertuokanashi Mn deposit.

Sample No.	Location	Rocks type	Total organic carbon content (wt%)	Pr/*n*-C_{17}	Ph/*n*-C_{18}	Pr/Ph	$\delta^{13}C_{v\text{-}PDB}$ (‰) of kerogen
OPM01-8	Hanging wall	Micrite	0.2	0.45	0.80	0.36	−27.9
OPM01-9	Hanging wall	Calcareous siltstone	0.5	0.55	0.99	0.29	−29.5
OPM01-15/1	Hanging wall	carbonaceous argillaceous limestone	0.7	0.54	1.19	0.34	−28.5
OPM01-15/2	Hanging wall	carbonaceous argillaceous limestone	0.4	0.46	0.88	0.33	−29.5
OPM01-15/3	Hanging wall	Calcareous siltstone	1.7	0.75	1.19	0.63	−29.5
OPM01-16	Ore-layer	Grey-black Mn ore	0.6	0.50	0.96	0.18	−27.9
OPM01-16/2	Ore-layer	Grey-black Mn ore	0.3	0.59	1.06	0.21	−29.5
OPM01-16/4	Ore-layer	Grey-black Mn ore	0.4	0.58	1.25	0.21	−29.9
OPM01-16/6	Ore-layer	Grey-black Mn ore	0.6	0.41	1.22	0.26	−29.2
OPM01-17	Footwall	Calcirudite	1.6	2.69	0.86	0.61	−28.5
OPM01-21	Footwall	Calcareous fine sandstone	0.5	0.62	1.39	0.41	−29.1

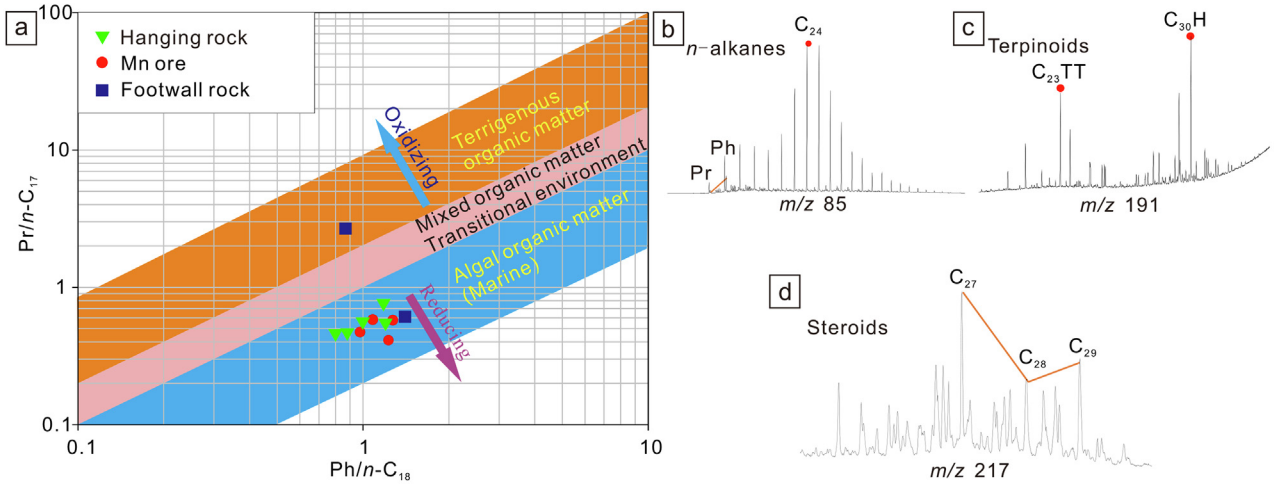

Fig. 7. A) pr/n-C_{17} versus Ph/n-C_{18} plot (after Shanmugam, 1985); b-d) The saturated hydrocarbon's gas chromatography-mass spectrometry of typical manganese ore.

Table 3
In-situ sulfur isotopes for the Aoertuokanashi Mn deposit, Western Kunlun Orogen.

Point No.	Mineral type	$\delta^{34}S_{V\text{-}CDT}$ (‰)
MN-01	Tabular Po	−5.6
MN-02		−6.2
MN-03		−8.4
MN-04		−7.4
Py-01	Hypidiomorphic granular Py	−4.5
Py-02		−5.1
Py-03		−7.3
Py-04		−7.9
Py-05		−5.3
Py-06		−5.9
Py-07		−5.8
Py-10		−3.5
Py-09	Globular Py	−38.7

Py = pyrite, and Po = Pyrrhotite.

6.7. Re-Os isotope composition

The Re and Os contents of eight Mn ore samples are 1.057–20.650 and 0.283–1.477 ppb, respectively with a Re/Os mass ratio of 1.7–59.9 (Table 4). The average content of Re and Os in the Re-Os dating samples is 8.701 and 0.592 ppb (Table 4), respectively. Using the ISOPLOT software of Ludwig (2003), the wide range in the ^{187}Re-^{187}Os values of the eight samples yielded a well-defined isochron with a weighted average age of 302 ± 9 Ma (MSWD = 22) and the initial $(^{187}Os/^{188}Os)_i$ range from 0.772 to 0.825 with a mean value of 0.789. This is interpreted as the age of the manganese mineralization (Fig. 8b).

7. Discussion

7.1. Geochronology for the Mn mineralization

The age of the basalt from the Wuluate Formation beneath the Mn deposit is ca. 313 ± 2 Ma (Yun, 2015; Ji et al., 2018). Thus, the age of the Mn is younger than this date (Fig. 8c). The age of the rhyolitic tuff sample from the Maerkanquekusaishan Formation overlying the Mn-rich units is 292 ± 3 Ma (Fig. 8a). Therefore, our data shows that the Mn mineralization at the Aoertuokanashi deposit is restrained between 313 and 292 Ma (Fig. 8c). The Re-Os weighted average age gives a concise date of 302 ± 9 Ma (MSWD = 22) for the mineralization (Fig. 8b), which is halfway between 313 and 292 Ma. This shows that the Mn at Aoertuokanashi was deposited in the Late Carboniferous.

Li et al. (2022a) reported a Re-Os isochron isotope age of 320 ± 7 Ma from Mn carbonate ores, but their detailed sample locations are not documented. This date is older than the ca. 313 Ma basalt in the Wuluate Formation at the footwall of the Mn-rich unit (Yun, 2015; Ji et al., 2018). Three pieces of evidence support the 302 ± 9 Ma Re-Os age for the Mn mineralization. Firstly, the Mn depositional age must be younger than the underlying volcanic rocks in the Wuluate Formation dated at 313 Ma. The second point of consideration is that the old age of the samples used by Li et al. (2022a) may have been weathered considering low Re and Os contents, 1.380 and 0.376 ppb, respectively in their samples. It is known that weathering can lead to the loss of Re and Os (Jaffe et al., 2002). To avoid this problem, fresh ore samples including four samples from the adit at an elevation of 3760 m were collected for Re-Os dating in this study. The average content of Re and Os in the Re-Os dating samples in this work is 8.701 and 0.592 ppb (Table 4), respectively, which are much higher than reported by Li et al. (2022a). The third point is that Re/Os ratios with a wide range of variation are easier and more accurately dated (Wu et al., 2021). The Re/Os mass ratio for our samples is 1.7–59.9, which is much wider that than of Li et al. (2022a) that ranges between 0.18 and 13.3 (Table 4). Thus, the age of the large Aoertuokanashi Mn deposit is 302 ± 9 Ma (Late Carboniferous).

7.2. Source of the Mn mineralization

The source of Mn-carbonate ore is still in dispute. Several possible sources of Mn include chemical weathering on continental margins (Calvert and Pedersen, 1996; Huckriede and Meischner, 1996; Maynard, 2010). Another possible source is from hot water along active faults and at volcanoes (Renard et al., 2005; Zhou et al., 2016; Maynard, 2014). Collier and Edmond (1984) estimate that the annual Mn content brought into the ocean by rivers is 3.4 x 10^5 t, hydrothermal vents (hot water) is 32–80 x 10^5 t, and the atmosphere is 0.6–1.6 x 10^5 t. Manganese from hydrothermal vents (hot water) accounts for ~ 90 % of the Mn sources in modern oceans, indicating that volcanic activity is a significant source of Mn into oceans. Maynard (2010) proposes that most economic Mn deposits come directly or indirectly from hydrothermal vents (hot water) associated with volcanism on the seafloor.

The enrichment of Fe and Mn in marine sediments is related to hydrothermal vents (hot water), whereas the Al content is related

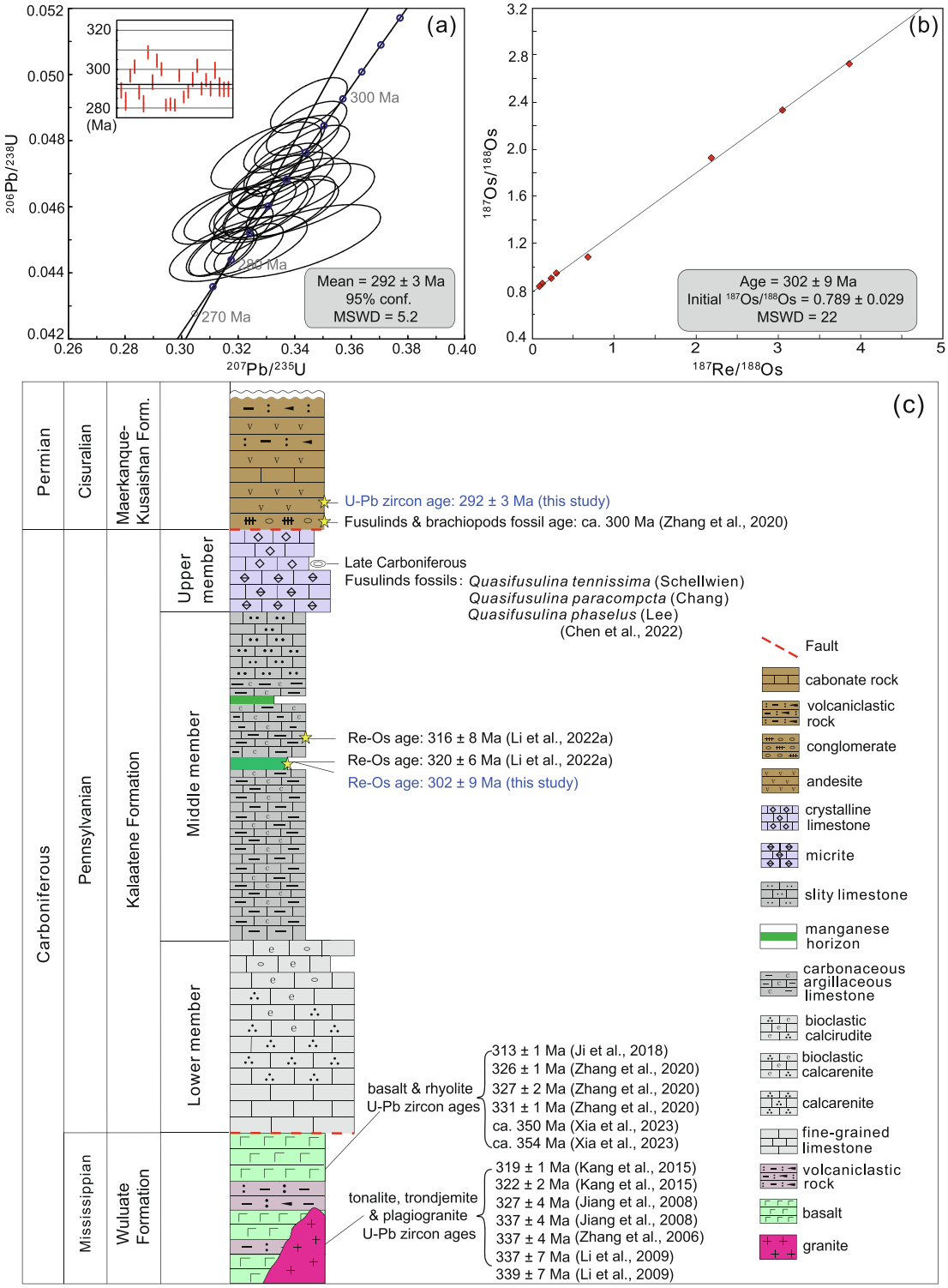

Fig. 8. Geochronology diagrams showing: a) zircon U-Pb isotope Concordia plot for rhyolitic tuff; b) Re-Os isochron diagram of organic matter in eight Mn ore samples from the Aoertuokanashi deposit; c) stratigraphic section of Mn-rich horizons and their country rocks with isotope ages. References for ages or fossil from: (Zhang et al., 2006; Jiang et al., 2008; Li et al., 2009; GSIHP, 2013; Kang et al., 2015; Ji et al., 2018; Zhang et al., 2020; Chen et al., 2022; Li et al., 2022a; Xia et al., 2023). Please refer to Supplementary Table 3 for the corresponding relationship between rock type and age.

to terrestrial sources. Therefore, the Al/(Al + Fe + Mn) mass ratio can be used to determine the contribution of hydrothermal vents (hot water). The Al/(Al + Fe + Mn) mass ratio of typical hot water sediment is < 0.35 (Boström, 1983). The Al/(Al + Fe + Mn) mass ratios of the Mn ore samples at Aoertuokanashi varies from 0.01 to 0.08 (Sup. Table S1). On the Fe-Mn-10 x (Cu + Ni + Co) diagram and the (Cu + Ni + Co)-Cu/Zn diagram (Fig. 9), all samples plot in the hydrothermal vents (hot water) field rather than hydrogenic sedimentary zone, indicating a hot water origin.

Deposits of volcanic or hydrothermal vents (hot water) are enriched in Cu and Ni and low in Co with Co/Ni mass ratios < 1 (Xie et al., 2006; Yang et al., 2010). Based on the geochemical char-

Table 4
Re-Os isotopic data for manganese ore from the Aoertuokanashi Mn deposit, Western Kunlun Orogen.

Sample No.	Sample Weight (g)	Re (ng/g)	Total Os (ng/g)	Common Os (ng/g)	^{187}Re (ng/g)	^{187}Os (ng/g)	^{187}Re/^{188}Os		^{187}Os/^{188}Os		$(^{187}Os/^{188}Os)_i$	Re/Os
							Ratio	2σ	Ratio	2σ		
OPM01-16	0.30098	20.650	0.420	0.329	12.980	0.099	305.30	3.10	2.335	0.004	0.795	49.2
OPM01-16/4	0.30034	2.714	0.600	0.532	1.706	0.064	24.08	0.26	0.908	0.003	0.787	4.5
OPM01-16/6	0.30091	12.490	0.341	0.267	7.854	0.070	218.00	2.60	1.925	0.016	0.825	36.6
OPM02-6/1	0.30048	6.220	0.496	0.407	3.909	0.063	68.15	1.09	1.088	0.012	0.744	12.5
3760/7/1	0.30055	1.236	0.514	0.463	0.777	0.053	12.71	0.13	0.865	0.002	0.801	2.4
3760/9/1	0.30028	1.057	0.606	0.540	0.665	0.060	9.18	0.12	0.837	0.008	0.791	1.7
3760/11/1	0.30045	8.263	1.477	1.340	5.193	0.166	29.86	0.31	0.951	0.002	0.800	5.6
3760/12/1	0.30090	16.980	0.284	0.213	10.670	0.075	386.50	3.90	2.722	0.004	0.772	59.9
Average	0.30060	8.701	0.592	0.511	5.469	0.080	131.72		1.450		0.789	14.7

Note: The location of samples OPM01-16, OPMO1-16/4, and OPMO1-16/6 is 39°20′17″N/73°40′19″E; the location of sample OPM02-6/1 is 39°20′31″N/73°38′36″E; and the location of the other samples is 39°20′25″N/73°40′02″E.

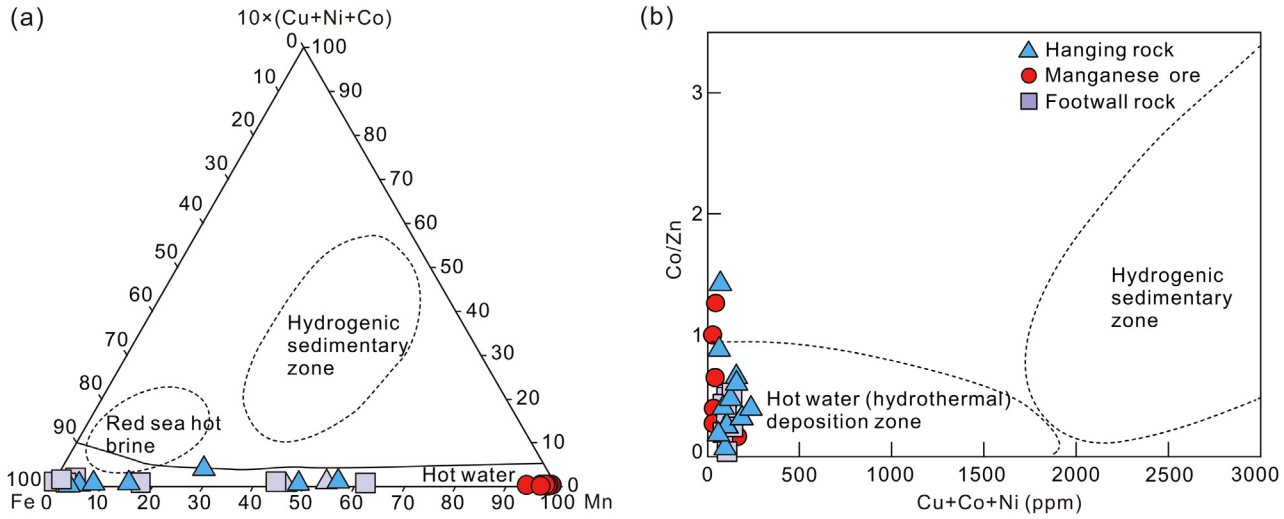

Fig. 9. Discrimination diagrams for the Mn); and b) Co/Zn mass ratio-(Cu + Ni + Co) diagrams (after). Source: a) mass ratios of Fe-Mn-10 x (Cu + Co + Ni) (after Bonatti, 1975Toth, 1980

acteristics of Mn deposits in China, Peng (1991) points out that the Co/Ni ratio is useful in estimating the distance from Mn sources, where Co/Ni mass ratios > 1 are considered to be a distal source and a mass ratio of < 0.55 for proximal sources. The Co/Ni mass ratio of the Aoertuokanashi Mn mineralization is 0.20–0.77 (only one sample is > 0.55), suggesting that the source of the Mn is a nearby volcano or hot water vent.

The basalt in the Wuluate Formation beneath the Mn-rich units is dated at 313 ± 2 Ma, and contains between 1000 and 1500 ppm Mn (Gao et al., 2018). The average Mn content of rocks of hot water precipitates in this formation is 3550 ppm. This is three times higher than that of the basalt (Gao et al., 2018), indicating that hot water activity likely contributed to Mn in the Aoertuokanashi deposit.

7.3. Metallogenic geological setting

Significant accumulations of Mn are reported in (1) Palaeoproterozoic, (2) Mesoproterozoic, (3) Neoproterozoic, (4) Silurian-Devonian, (5) Permian, (6) Middle to Late Mesozoic, and (7) Early Cenozoic (Roy, 2006; Nakagawa et al., 2009; Kuleshov, 2011; De Putter and Ruffet, 2020). The Late Carboniferous Aoertuokanashi Mn deposit is the first large high-grade carbonate-hosted deposit of such age in the world.

The tectonic evolution of the WKO has involved the opening and closing of the Proto-Tethys and Paleo-Tethys oceans during the Early Paleozoic (Jiang et al., 1992; Matte et al., 1996; Mattern and Schneider, 2000; Xiao et al., 2002, 2005; Pan and Fang, 2010; Dong et al., 2021, 2022). Plate collision marked the closure of the Proto-Tethys Ocean (Jiang et al., 2008; Liao et al., 2010; Jia et al., 2013; Liu et al., 2014; Zhang et al., 2019). This was followed by the opening and closure of the Paleo-Tethys Ocean during the Late Paleozoic (Matte et al., 1996; Mattern and Schneider, 2000; Wang, 2004; Xiao et al., 2005; Jiang et al., 2008).

In the North WKO, the 313 Ma volcanic rocks in the Wuluate Formation are overlain by the Mn-bearing layers, and the Wuluate Formation is considered to have formed in a back-arc basin due to the northward subduction of the Paleo-Tethys Ocean (Yun, 2015; Ji et al., 2018; Xia et al., 2023) (Fig. 10). The back-arc environment is considered to be a favorable setting for Mn deposits (West et al., 2008; Rubinstein and Zappettini, 2015), such as in the modern southwestern Pacific Ocean (Pelleter et al., 2017). The Qaidam Block and North China Block were in the northern part of the Paleo-Tethys Ocean along with the Tarim Block during the Late Carboniferous (Fig. 10a). A back-arc environment existed at the Qaidam Block and North China Block due to the northward subduction of the Paleo-Tethys oceanic crust (Wang et al., 2016; Sun et al., 2022; Liu et al., 2023a). There is no report, however, of the pres-

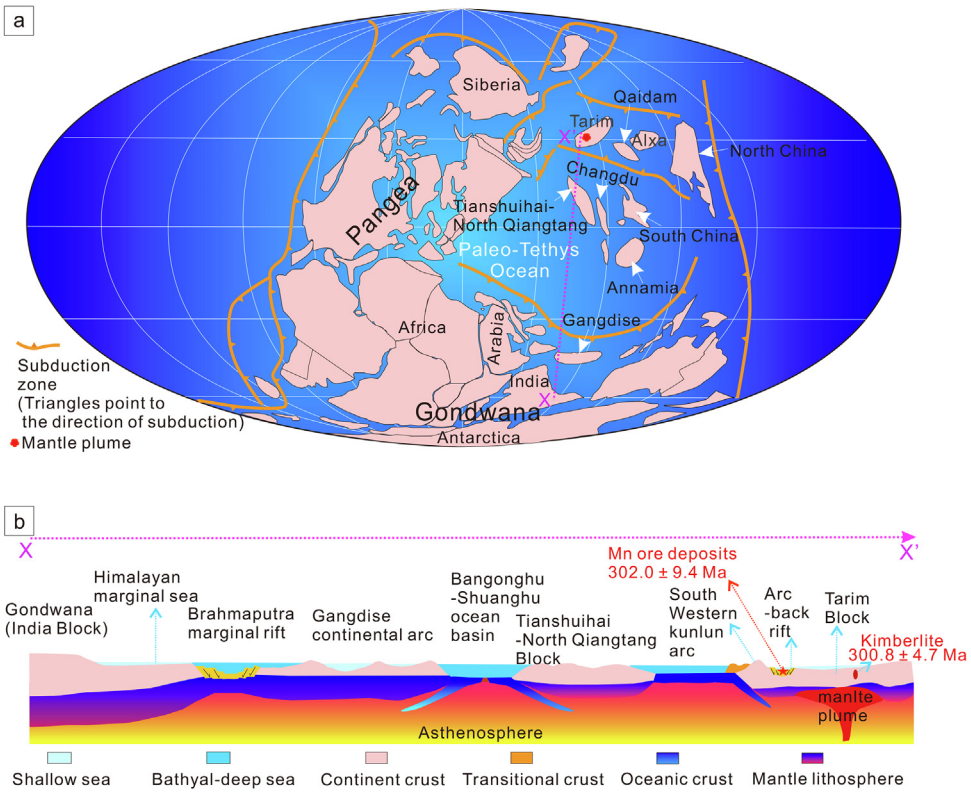

Fig. 10. The geological background of the Aoertuokanashi Mn ore deposit: a) the Late Carboniferous paleogeographic reconstruction showing simplified plate boundaries (modified after Blakey, 2011; Li et al., 2011; Domeier and Torsvik, 2014; Huang et al., 2018); and b) Late Carboniferous tectonic of Gondwana and the Tarim Block.

ence of Mn deposits in these back-arc basins. There must be a unique geological factor in the WKO that has resulted in the deposition of Mn in the back-arc setting during the Late Carboniferous. We propose that the upwelling of a mantle plume may have contributed to the Mn mineralization based on the following evidence:

Ⅰ. The Mn mineralization age of 302 ± 9 Ma is the same within error as the age of the 301 ± 5 Ma Wajilitag kimberlite intrusions in the Tarim Block, and the Wajilitag kimberlite intrusion is believed to be the initial magmatic pulse triggered by Tarim mantle plume (Fig. 1b; Zhang et al., 2013).

Ⅱ. Flood basalt has recently been recognized in the North Qiangtang region. The basalt erupted during ca. 295–284 Ma covering an area of 105 km^2 with a maximum thickness of 2 km and is thought to be the result of the Tarim mantle plume (Zhang and Zhang, 2017). The North WKO back-arc basin is between the Tarim Block and the North Qiangtang (Fig. 10b). It is, therefore, reasonable to consider that the Tarim mantle plume had an impact on the nearby North WKO back-arc basin during the Late Carboniferous (Fig. 10a, b).

Ⅲ. Significantly lower $(^{187}Os/^{188}Os)_i$ values of 0.28–0.38 have been observed for the footwall at the Aoertuokanashi deposit (Li et al., 2022a). Although the values are higher than the mantle values (0.1–0.15), they are much lower than average crustal rocks ranging between 1 and 2 (Reisberg and Meisel, 2002). The data suggest a contribution of mantle-derived Os into the North WKO back-arc basin (Li et al., 2022a).

Ⅳ. The Wuzibielishankou-Akecheyi Fault (known as the Kegang Fault to the east) forms the boundary between the Tarim Block and the North WKO back-arc basin (Fig. 1b, c). The fault is a lithospheric fault that existed during the Early Carboniferous and is located in the transition zone of the Moho surface in the WKO. The depth of the Moho surface in the north and south of the fault is about 50 km and 70 km, respectively (Zhang et al., 2022), indicating that it can provide channels for mantle-derived materials.

Based on these observations, it is proposed that large-scale Late Carboniferous Mn mineralization in the WKO was associated with the back-arc environment, itself influenced by the Tarim mantle plume. The link between carbonate-hosted Mn deposit and the mantle plume can be found not only in the area around the Tarim mantle plume but also within the influence range of the Emeishan mantle plume. Strontium and Hg isotopes show that the Middle Permian Zunyi rhodochrosite deposit in China is related to the Emeishan mantle plume, and the age of this Mn deposit is consistent with that of the basalt in the early stage of the Emeishan mantle plume (Xu et al., 2021; Yan et al., 2023; Yang et al., 2023).

7.4. Microbial mediation and redox state of the depositional environment

Previous studies have shown that Mn deposition is related to microbial activity (Polgári et al., 2016; Biondi and Lopez, 2017). Soluble Mn (II) can be oxidized to Mn (III/IV) oxides by a microbially mediated process (Nealson et al., 1988; Tebo et al., 2004; Webb et al., 2005). Manganese (IV) oxide can be reduced by bacteria to form Mn (II) carbonate or Mn (II) silicate (Thamdrup, 2000; Johnson et al., 2016). Globular pyrite is developed at the Aoertuokanashi deposit with a $\delta^{34}S$ value of −38.7 ‰ (Supplementary Fig. 2f), indicating that sulfate reducing microorganisms played a role during mineralization and that sulfate concentrations were higher than 0.2 mM (Habicht et al., 2002). The sedimentary facies of the lower, middle, and upper members of the Kalaatehe formation are platform shoal facies, tidal flat facies or restricted platform facies, and open platform facies, respectively (Fig. 4). It means that the sedimentary environment gradually becomes deeper, which is

the feature of a starving basin. Starving basin is favorable for microbial mediation (Polgári and Gyollai, 2022). Lamina occurrence and biomat were observed in Mn ores (Fig. 5d and e), which also support the microbial contribution. Besides, authigenic quartz featured by non-luminescence under cathodoluminescence microscopy can be produced in microbially mediated diagenetic processes (Marshall, 1998; Amores and Warren, 2007; Polgári et al., 2019). Authigenic quartz has been observed in Mn ore samples (Supplementary Fig. 1), supporting the interpretation that microbial mediation existed.

Manganese is a redox-sensitive element as it shows variable oxidation states, and its mineralization is closely related to redox condition, which also has an important impact on microbial mediation. The ∑REE content, 44–284 ppm, of the Mn mineralization in the study area is much higher than that of the footwall and hanging wall and is similar to those of marine sedimentary carbonate rocks. In Fig. 6, the Mn ore samples collected for this study are positively anomalous in Ce, which is a typical feature of modern submarine manganese nodules. Under oxidizing conditions, the soluble Ce^{3+} ion is easily oxidized by Mn-oxidizing microbes to insoluble Ce^{4+} ion. The insoluble Ce^{4+} ion is adsorbed by fine-grained nodules containing Fe-Mn hydroxide on the seafloor, which results in positive Ce anomalies in Fe-Mn nodules (Høgdahl et al., 1968; Elderfield et al., 1981; Pattan and Parthiban, 2011; Li et al., 2020; Polgári and Gyollai, 2022). The Mn mineralization at the Aoertuokanashi deposit shows positive Ce anomalies (Fig. 6), indicating that Mn was deposited in an oxic environment.

Hatch and Leventhal (1992) compared V/(V + Ni) mass ratios to other geochemical redox indicators and suggested ratios greater than 0.84 for euxinic conditions, 0.54–0.82 for anoxic waters, 0.46–0.60 for dysoxic conditions, and less than 0.46 for oxic environment. The average V/(V + Ni) mass ratio of seven Mn ore samples collected from the Aoertuokanashi deposit is 0.39, which indicates that the Mn was deposited in an oxic environment. Obligatory oxic conditions are needed for the Mn precipitation from dissolved Mn(II), because the microbial multicopper oxidase enzymatic process during Mn precipitation is active only under aerobic conditions (Brouwers et al., 2000; Bargar et al., 2005). A biologically formed Mn(III) or Mn (IV) oxide (e.g., birnessite) is the first product of microbial enzymatic Mn(II) oxidation (Butterfield et al., 2013; Polgári and Gyollai, 2022). This enzymatic Mn oxidation is Cycle I (Mn^{2+}→Mn^{4+}) in Mn ore formation (Polgári and Gyollai, 2022). According to the Mn^{2+}-Mn^{4+} coexist oxygen buffer (Huebner and Sato, 1970), the oxygen fugacity value of Cycle I was above FMQ + 6.4 (FMQ = fayalite–magnetite–quartz redox buffer, in log fo_2) at 2 MPa and 300 K.

Although the manganese ore has undergone an oxic stage (Cycle I), the organic geochemical characteristics show that there was an anoxic stage (Cycle II, Mn^{4+}→Mn^{2+}). Phytols formed by microorganisms, such as chlorophyll in higher plants and phycocyanin in algae, transforms into pristane (Pr) in sub-oxic acidic medium, and transforms into phytane (Ph) in anoxic alkaline medium (Peters and Moldowan, 1993). Peters and Moldowan (1993) summarized that Pr/Ph mass ratios < 0.8 indicate a highly-anoxic environment, Pr/Ph ranges from 0.8 to 3 represent an anoxic environment, and Pr/Ph mass ratios > 3 point to an oxic environment. The Pr/Ph mass ratios of the floor rocks, Mn ores, and roof rocks are 0.29–0.63, 0.18–0.26, and 0.41–0.61, respectively (Table 2), which indicates a highly-anoxic environment. On the cross plot of Pr/n-C_{17} and Ph/n-C_{18} (Fig. 7a), all Mn ore samples and hanging rocks are located in the reducing marine algal organic matter zone, only one footwall rock plots in the oxidized terrigenous organic matter zone. Gypsum was a product of the second metallogenic period, because it form cross-cutting veins (Fig. 5k), and both gypsum and sulfides are retained in the ore samples (Fig. 5h and k), so the oxygen fugacity of Cycle II can be roughly constrained by the oxygen fugacity represented by the coexistence of gypsum and sulfides. According to the sulfide-gypsum equilibrium oxygen fugacity buffer provided by Liu et al. (2023b), its oxygen fugacity value was FMQ + 4.5 at 2 MPa and 300 K. This oxygen fugacity is much lower than that of Cycle I (FMQ + 6.4), indicating that reduction occurred. Reduction perhaps occurred via diagenesis, because of organic matter accumulation. Organic matter probably comes from two sources. One is marine algae, as the GC–MS result of saturated hydrocarbons in the ore samples shows that there are organic components of marine algae (Fig. 7a). The second possible source is microorganisms, because pyrite with a $\delta^{34}S$ value of −38.7 ‰ (Supplementary Fig. 2) and typical biomat (Fig. 5e) are observed in ore samples.

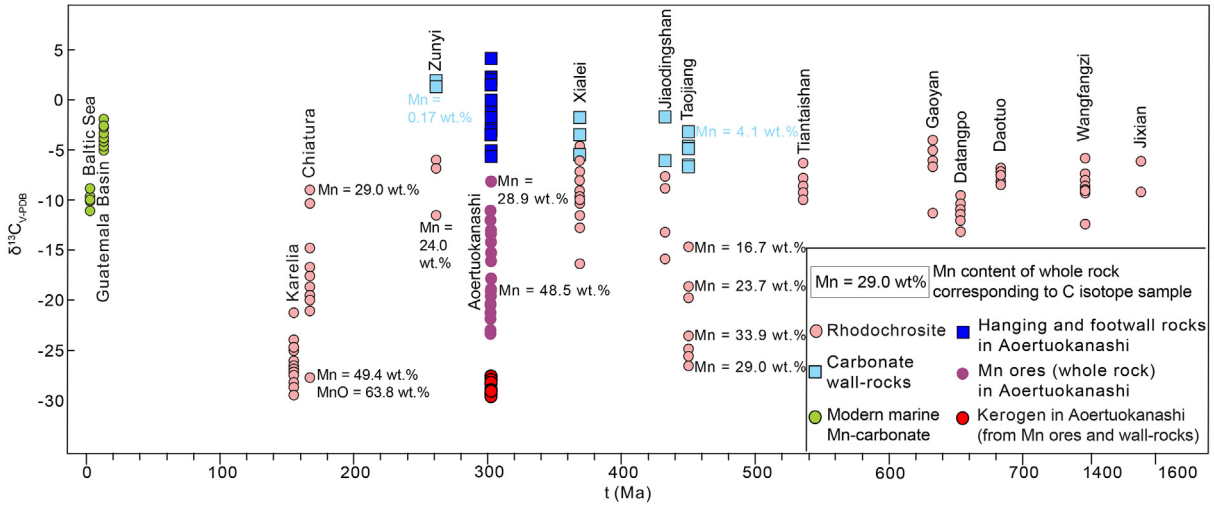

Fig. 11. Distribution of carbon isotopes from manganese deposits in the world. The Zunyi data is from Jiang et al. (2016); the Xialei data is from Qin et al. (2010); the data for Jixian is from Fan et al., (1999a); the data for Wangfangzi is from Fan et al., (1999b); the data for Jiaodingshan, Taojiang, Tiantaishan, Gaoyan, and Datangpo is from Fan et al. (2004); Daotuo data is from An et al. (2014); the data for Chiatura is from Kuleshov et al. (2023); and the data for Baltic Sea, Guatemala Basin, and Karelia is from Kuleshov (2017).

7.5. The role of organic matter at the Aoertuokanashi Mn deposit

Manganese has + 2, +3, +4, and + 7 oxidation states in nature. As mentioned earlier, the enrichment and precipitation of Mn are thought to be controlled by redox conditions (Nakagawa et al., 2009). Under oxic conditions, Mn^{2+} will dissolve in water, while Mn^{4+} will precipitate forming pyrolusite (MnO_2) and manganite (hydroxide). Under anoxic conditions, Mn^{4+} ions are reduced to Mn^{2+} ions which, in the presence of CO_3^{2-}, will precipitate as Mn carbonate (Canfield et al., 2005; Maynard, 2010, 2014; Nakagawa et al., 2009; Wang et al., 2018; Yin and Xiao, 2014). In oxic and anoxic stratified water, Mn^{2+} ions will precipitate forming oxides or hydroxides at the oxic-anoxic interface. When organic-rich sediments are deposited, Mn oxides and hydroxides interact with organic matter, which releases Mn^{2+} ions in pore waters of the reducing environment. The ions will then combine with CO_3^{2-} produced from the oxidation of organic matter which results in the precipitation of Mn carbonate (Calvert and Pedersen, 1993, 1996; Roy, 2006; Maynard, 2014).

The $\delta^{13}C_{V\text{-}PDB}$ values of carbonate in the footwall rocks at the Aoertuokanashi deposit range from −5.3 to 1.5 ‰, whereas the Mn carbonate in the mineralization unit are much more ^{13}C-depleted and range from −19.5 to −8.2 ‰. This is also more ^{13}C-depleted than the hanging rocks, which have $\delta^{13}C_{V\text{-}PDB}$ values from −5.1 to + 4.2 ‰ (Table 1). The overall $\delta^{13}C_{V\text{-}PDB}$ values of normal Late Carboniferous marine carbonates vary from −2.5 to + 5 ‰ (Grossman et al., 2008; Liu et al., 2017). Fig. 11 shows that the $\delta^{13}C_{V\text{-}PDB}$ values of the rock bordering the Mn mineralization are within this expected marine Mn-carbonate range. Hence, the $\delta^{13}C_{V\text{-}PDB}$ values of the Mn mineralization are significantly ^{13}C-depleted compared to normal marine carbonate, and instead are in the range of organic matter. This indicates that organic matter played a role in the formation of the Mn deposit. After its oxidation, organic matter can cause a strong negative shift in carbon isotope values (Frimmel, 2010). The kerogen (organic matter) $\delta^{13}C_{V\text{-}PDB}$ value is around −29 ‰, which is significantly lower than that of the whole rock (Tables 1 and 2, Fig. 11). A reasonable explanation is that pre-existing Mn oxide (or hydroxide) was reduced by organic matter (Veglio and Toro, 1994; Morad and Al-Aasm, 1997; Johnson et al., 2013). Thus, it is reasonable that the Mn ore at Aoertuokanashi was deposited according to the reaction $Mn^{2+} + CO_3^{2-} \rightarrow MnCO_3$ (rhodochrosite). The $\delta^{13}C_{V\text{-}PDB}$ values of the large

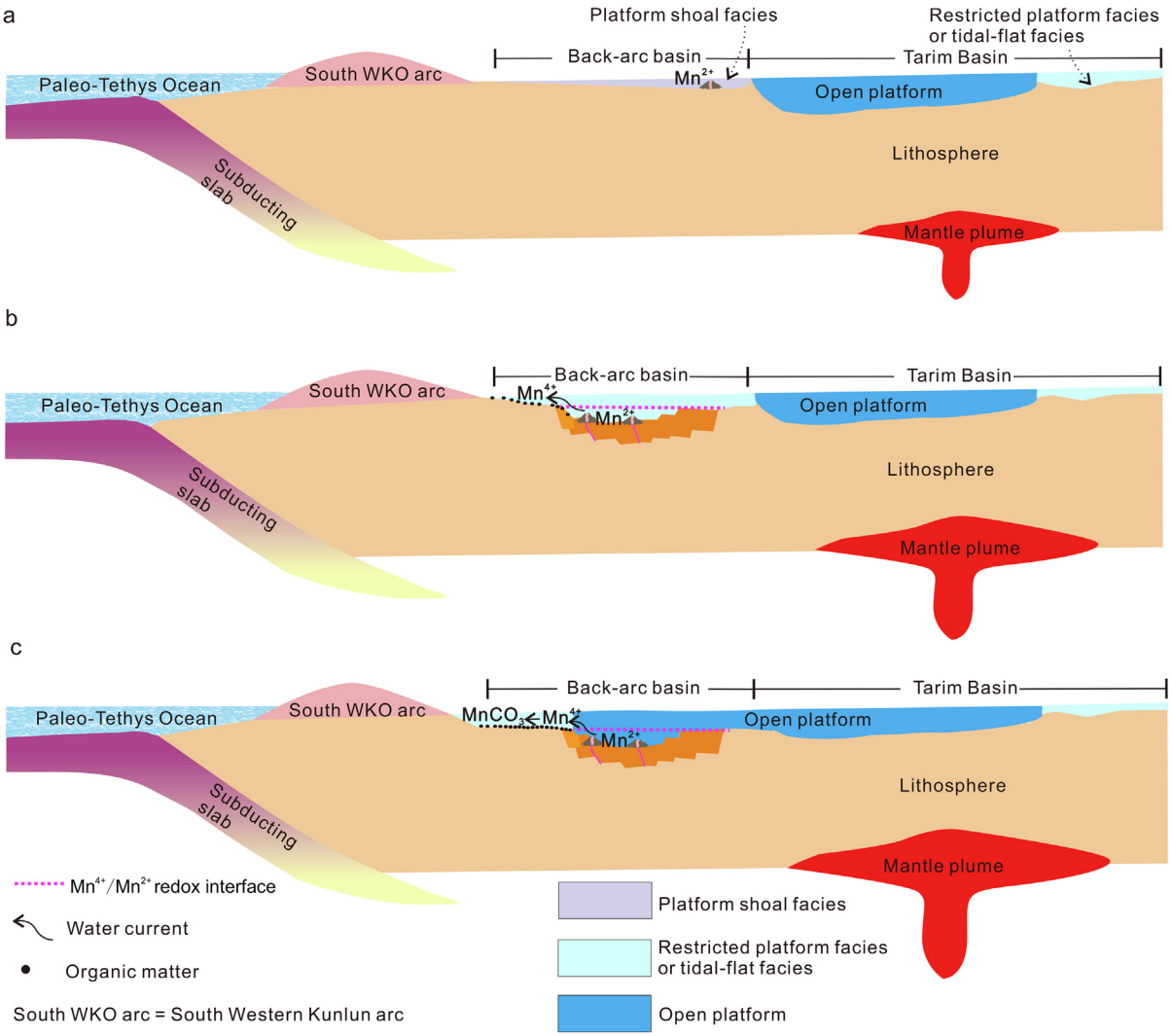

Fig. 12. Metallogeny model of the Late Carboniferous Aoertuokanashi Mn deposit in the Western Kunlun Orogen showing: a) the deposition of the lower member of Kalaatehe Formation in the North WKO back-arc basin; b) the deposition of the middle member of Kalaatehe Formation in the back-arc basin; and c) transitions from the middle to the upper member of the Kalaatege Formation. Note: The unit deposited in the Tarim Basin in the above figures is the Xiaohaizi Formation. During the Late Carboniferous, the Tarim Basin was shallow to the north and deep in the southwest (Li et al., 2014).

Aoertuokanashi and Taojiang deposits (grading between 25 and 35 wt% Mn) are lower than those grading < 25 wt% Mn, such as the Zunyi, Xialei, Jiadingshan, Tiantaishan, Gaoyan, Datangpo, Wafangdian, and Daotuo deposits, but they are similar to Mn deposits with high Mn grades elsewhere in the world, such as the Karelia and Chiatura deposits (Fig. 11). In summary, the reductive power of organic matter is an important mechanism for the formation of the high-grade carbonate-hosted Aoertuokanashi Mn deposit.

8. Proposed model

The WKO had a complex history since the Early Carboniferous. The North WKO back-arc basin was formed during the Late Carboniferous with the initial widespread deposition of a thick mafic volcanic sequence (Yun, 2015). During this period, the lower member of the Kalaatehe Formation (platform shoal facies) formed in the back-arc environment. The Xiaohaizi Formation representing carbonate shoals and lagoons in a mixed siliciclastic-carbonate platform deposited in the Tarim Basin to the northeast (Zhu et al., 2002; Li et al., 2014). This shows that a shallow sedimentary sequence was deposited in the northeast and a deeper sedimentary sequence in the southwest. The Late Carboniferous sedimentary units in the Tarim Basin were deposited in a restricted and open platform environment (Zhu et al., 2002; Li et al., 2014). During the Late Carboniferous, the Tarim mantle plume probably caused significant submarine hydrothermal activity (hot water), which delivered a large amount of Mn^{2+} into the North WKO back-arc basin (Fig. 12a).

During gradual subsidence, the sea level in the North WKO back-arc basin area slowly rose, and restricted platform or tidal-flat facies formed (Fig. 12b). Organic matter and Mn^{2+} were continually enriched in the back-arc basin. Fluid circulation in the basin resulted in the movement of dissolved Mn into the upper oxygen-rich environment where the Mn^{2+} ion was transformed to Mn^{4+} by microbial mediation. In this way, Mn oxides or hydroxides were deposited (Fig. 12b).

As the sea level continued to rise, the redox front also rose, and deeper waters became anoxic or dysoxic (Fig. 12c). In this environment, the carbonaceous argillaceous limestone with high organic matter content and framboidal pyrite were deposited. The Mn oxides reacted with organic matter converting Mn^{4+} to Mn^{2+} and reacted with the organic matter forming CO_3^{2-} ions. The subsequent reaction of Mn^{2+} with CO_3^{2-} resulted in the deposition of rhodochrosite (Fig. 12c).

9. Conclusions

The age of the Aoertuokanashi Mn deposit is 302 ± 9 Ma (MSWD = 22). This is the first Late Carboniferous high-grade and large carbonate-hosted Mn deposit recognised in the world. Manganese was deposited in the North WKO back-arc basin during the northward subduction of the Paleo-Tethys Ocean. The Tarim mantle plume promoted Mn mineralization through hydrothermal activity. The restricted platform or tidal flat facies is favorable sedimentary environment for carbonate-hosted manganese deposits. Microorganisms played an important role in the formation of tetravalent manganese. The reduction of marine organic matter led to the formation of carbonate manganese ore.

In an extensional environment within the influence range of a mantle plume, the strata with strong hot water activities and a large amount of organic matter is the priority position for the formation of carbonate type manganese ore.

CRediT authorship contribution statement

Yongbao Gao: Writing – review & editing, Writing – original draft, Visualization, Validation, Supervision, Software, Resources, Methodology, Investigation, Funding acquisition, Formal analysis, Data curation, Conceptualization. **Leon Bagas:** Writing – review & editing, Writing – original draft, Validation, Methodology. **Yuegao Liu:** Writing – review & editing, Writing – original draft, Visualization, Validation, Software, Resources, Methodology, Investigation, Funding acquisition, Formal analysis, Data curation, Conceptualization. **Wenyuan Li:** Supervision, Methodology. **Keiko Hattori:** Writing – review & editing, Validation, Methodology. **Dominic Papineau:** Writing – review & editing, Software, Investigation. **Delong Jing:** Visualization, Software, Methodology, Investigation. **Denghui Chen:** Methodology, Investigation. **Jiaxin Teng:** Investigation. **Yongkang He:** Investigation. **Min Zhao:** Investigation. **Long Zhang:** Validation, Software. **Zhe Zhao:** Visualization, Methodology.

Declaration of competing interest

The authors declare that they have no known competing financial interests or personal relationships that could have appeared to influence the work reported in this paper.

Acknowledgments

We thank the associate editor Professor Jan Marten Huizenga - for the meticulous and rigorous suggestions. We are very grateful to Professor Wenjiao Xiao and other anonymous reviewers for improving this manuscript and constructive opinions. This research was financially supported by National Natural Science Foundation of China (92262302), the Second Tibetan Plateau Scientific Expedition and Research (STEP) (2019QZKK0806), Natural Science Basic Research Program of Shaanxi (2023-JC-YB-241), Projects DD20160004, DD20190143, DD20230060 and DD20230378 at China Geological Survey, the Hainan Provincial Joint Project of Sanya Yazhou Bay Science and Technology City (2021CXLH0027), and the New Star of South China Sea Talent Project (NHXXRCXM202339). We thank Professors Chao Li and Chuanzhou Liu for their assistance in processing and interpreting Re-Os isotope data. Professor Yuanjia Han helped a lot in organic geochemical analysis.

Appendix A. Supplementary data

Supplementary data to this article can be found online at https://doi.org/10.1016/j.gr.2024.06.006.

References

Amores, D.R., Warren, L.A., 2007. Identifying when microbes biosilicify: the interconnected requirements of acidic pH, colloidal SiO_2 and exposed microbial surface. Chem. Geol. 240, 298–312.

An, Z.Z., Zhang, R.B., Chen, J.C., Qin, Y., Pan, W., Wu, G.W., Peng, Q.Y., Zheng, C., Zhang, F.F., Zhu, X.K., Wang, H.B., 2014. Geological and geochemical characteristics of Daotuo superlarge manganese ore deposit in Songtao County of Guizhou Province: Constraint on formation mechanism of Mn carbonate ores. Miner. Deposits 33, 870–884. In Chinese with English abstract.

Bargar, J.R., Tebo, B.M., Bergmann, U., Webb, S.M., Glatzel, P., Chiu, V.Q., Villalobos, M., 2005. Biotic and abiotic products of Mn (II) oxidation by spores of the marine Bacillus sp. strain SG-1. Am. Mineral. 90, 143–154.

Blakey, R.C., 2011. Mollewide plate tectonics maps: Pennsylvanian. Retrieved from. http://cpgeosystemscom/300moll.jpg.

Biondi, J.C., Lopez, M., 2017. Urucum Neoproterozoic-Cambrian manganese deposits (MS, Brazil): Biogenic participation in the ore genesis, geology, geochemistry, and depositional environment. Ore Geol. Rev. 91, 335–386.

Bonatti, 1975. Metallogenesis at Oceanic Spreading Centers. Annu. Rev. Earth Planet. Sci. 3, 401–431.

Boström, K., 1983. Genesis of ferromanganese deposits-diagnostic criteria for recent and old deposits. Springer, US.
Brouwers, G.J., Vijgenboom, E., Corstjens, P., De Vrind, J., De Vrind-De Jong, E., 2000. Bacterial Mn^{2+} oxidizing systems and multicopper oxidases: an overview of mechanisms and functions. Geomicrobiol. J. 17, 1–24.
Butterfield, C.N., Soldatova, A.V., Lee, S.-W., Spiro, T.G., Tebo, B.M., 2013. Mn (II, III) oxidation and MnO_2 mineralization by an expressed bacterial multicopper oxidase. Proc. Natl. Acad. Sci. u.s.a. 110, 11731–11735.
Calvert, S.E., Pedersen, T.F., 1993. Geochemistry of Recent oxic and anoxic marine sediments: Implications for the geological record. Mar. Geol. 113, 67–88.
Calvert, S.E., Pedersen, T.F., 1996. Sedimentary geochemistry of manganese; implications for the environment of formation of manganiferous black shales. Econ. Geol. 91, 36–47.
Canfield, D.E., Erik, K., Bo, T., 2005. The Iron and Manganese Cycles. In: Canfield, D.E., Kristensen, E., Thamdrup, B. (Eds.), Advances in Marine Biology. Academic Press, pp. 269–312.
Chen, D.H., Sui, Q.L., Zhao, X.J., Jing, D.L., Teng, J.X., Gao, Y.B., 2019. Geology, geochemical characteristics, and sedimentary environment of Mn-bearing carbonate from the Late Carboniferous Muhu manganese deposit in West Kunlun. Acta Sedimentol. Sin. 37, 477–490. In Chinese with English abstract.
Chen, D.H., Sui, Q.L., Guo, Z.P., Zhao, X.J., Teng, J.X., Gao, Y., 2022. Sedimentary environment of Mn-bearing carbonate from the Muhu manganese deposit in Malkansu, West Kunlun: Evidences from Fusulinids and C-O-Sr isotopes. Northwest. Geol. 55, 1–13. In Chinese with English abstract.
Chen, F., Wang, Q., Pufahl, P.K., Matheson, E.J., Xian, H., Nan, J., Ma, H., Deng, J., 2023. Carbonate-hosted manganese deposits and ocean anoxia. Earth Planet. Sci. Lett. 622, 118385.
Collier, R., Edmond, J., 1984. The trace element geochemistry of marine biogenic particulate matter. Prog. Oceanogr. 13, 113–199.
De Putter, T., Ruffet, G., 2020. Supergene manganese ore records 75 Myr-long Campanian to Pleistocene geodynamic evolution and weathering history of the Central African Great Lakes Region-Tectonics drives, climate assists. Gondwana Res. 83, 96–117.
Ding, L., Li, Z., Song, P., 2017. Core fragments of Tibetan Plateau from Gondwanaland united in northern hemisphere. Bulletin of Chinese Academy of Sciences (chinese Version) 32, 945–950. In Chinese with English abstract.
Domeier, M., Torsvik, T.H., 2014. Plate tectonics in the late Paleozoic. Geosci. Front. 5, 303–350.
Dong, Y., Sun, S., Santosh, M., Hui, B., Sun, J., Zhang, F., Cheng, B., Yang, Z., Shi, X., He, D., 2022. Cross Orogenic Belts in Central China: Implications for the tectonic and paleogeographic evolution of the East Asian continental collage. Gondwana Res. 109, 18–88.
Dong, Y., Sun, S., Santosh, M., Zhao, J., Sun, J., He, D., Shi, X., Hui, B., Cheng, C., Zhang, G., 2021. Central China orogenic belt and amalgamation of East Asian continents. Gondwana Res. 100, 131–194.
Elderfield, H., Hawkesworth, C.J., Greaves, M.J., Calvert, S.E., 1981. Rare earth element zonation in Pacific ferromanganese nodules. Geochim. Cosmochim. Acta 45, 1231–1234.
Fan, D., Yang, P., Wang, R., 1999a. Characteristics and origin of the middle Proterozoic Dongshuichang chambersite deposit, Jixian, Tianjin. China. Ore Geol. Rev. 15, 15–29.
Fan, D., Ye, J., Li, J., 1999b. Geology, mineralogy, and geochemistry of the Middle Proterozoic Wafangzi ferromanganese deposit, Liaoning Province. China. Ore Geol. Rev. 15, 31–53.
Fan, D.L., Zhang, T., Ye, J., 2004. The black shale series in China and its mineral deposits. Science Press, Beijing (In Chinese with English abstract).
Frimmel, H.E., 2010. On the reliability of stable carbon isotopes for Neoproterozoic chemostratigraphic correlation. Precambrian Res. 182, 239–253.
Gao, Y.B., Teng, J.X., Chen, D.H., Sui, Q.L., 2017. Metallogenic Geological Characteristics and Prospecting Direction of Maerkansu Manganese Ore Belt in West Kunlun. Xinjiang. Northwest. Geol. 050, 261–269. In Chinese with English abstract.
Gao, Y.B., Teng, J.X., Li, W.Y., Chen, D.H., Sui, Q.L., Jing, D.L., He, Y.K., Bai, J.K., 2018. Geology, geochemistry and ore genesis of the Aoertuokanashi manganese deposit, western Kunlun, Xinjiang. Northwest China. Acta Petrol. Sin. 34, 2341–2358. In Chinese with English abstract.
Grossman, E.L., Yancey, T.E., Jones, T.E., Bruckschen, P., Chuvashov, B., Mazzullo, S., Mii, H.S., 2008. Glaciation, aridification, and carbon sequestration in the Permo-Carboniferous: the isotopic record from low latitudes. Palaeogeogr., Palaeoclimatol. Palaeoecol. 268, 222–233.
GSIHP (Geological Survey Institute of Henan Province), 2013. 1:50000 Karagayiqiati, Kiyazi, Malitabaer Mountain, Botoyan, and Muhu Regional Geological Survey Report.
Habicht, K.S., Gade, M., Thamdrup, B., Berg, P., Canfield, D.E., 2002. Calibration of sulfate levels in the Archean ocean. Science 298, 2372–2374.
Han, Y., Zhao, G., Cawood, P.A., Sun, M., Eizenhöfer, P.R., Hou, W., Zhang, X., Liu, Q., 2016. Tarim and North China cratons linked to northern Gondwana through switching accretionary tectonics and collisional orogenesis. Geology 44, 95–98.
Hatch, J.R., Leventhal, J.S., 1992. Relationship between inferred redox potential of the depositional environment and geochemistry of the Upper Pennsylvanian (Missourian) Stark Shale Member of the Dennis Limestone, Wabaunsee County, Kansas, U.S.A. Chem. Geol. 99, 65–82.
Høgdahl, O.T., Melsom, S., Bowen, V.T., 1968. Neutron Activation Analysis of Lanthanide Elements in Sea Water. In: Baker, R.A. (Ed.), Trace Inorganics in Water. American Chemical Society, Miami Beach, pp. 308–325.
Huang, B., Yan, Y., Piper, J.D., Zhang, D., Yi, Z., Yu, S., Zhou, T., 2018. Paleomagnetic constraints on the paleogeography of the East Asian blocks during Late Paleozoic and Early Mesozoic times. Earth-Sci. Rev. 186, 8–36.
Huckriede, H., Meischner, D., 1996. Origin and environment of manganese–rich sediments within black–shale basins. Geochim. Cosmochim. Acta 60, 1399–1413.
Huebner, J.S., Sato, M., 1970. The oxygen fugacity-temperature relationships of manganese oxide and nickel oxide buffers. Am. Mineral. 55, 934–952.
Jaffe, L.A., Peucker-Ehrenbrink, B., Petsch, S.T., 2002. Mobility of rhenium, platinum group elements and organic carbon during black shale weathering. Earth Planet. Sci. Lett. 198, 339–353.
Ji, W.H., Chen, S.J., Li, R.S., He, S.P., Zhao, Z.M., Pan, X.P., 2018. The origin of Carboniferous-Permian magmatic rocks in Oytag area, West Kunlun: Back-arc basin? Acta Petrol. Sin. 34, 2393–2409. In Chinese with English abstract.
Jia, R.Y., Jiang, Y.H., Liu, Z., Zhao, P., Zhou, Q., 2013. Petrogenesis and tectonic implications of early Silurian high-K calc-alkaline granites and their potassic microgranular enclaves, western Kunlun orogen, NW Tibetan Plateau. Int. Geol. Rev. 55, 958–975.
Jiang, R., Fu, Y., Xu, Z.G., Pei, H.X., Wang, F.L., Xi, Z.W., 2016. Geochemical Constraints on the manganese mineralization during the Latest Maokou Epoch of Permian—example from the Nancha manganese ore deposit in Zunyi city, northern Guizhou. Acta Sedimentol. Sin. 34, 1032–1043. In Chinese with English abstract.
Jiang, Y.H., Liao, S.Y., Yang, W.Z., Shen, W.Z., 2008. An island arc origin of plagiogranites at Oytag, western Kunlun orogen, northwest China: SHRIMP zircon U-Pb chronology, elemental and Sr-Nd-Hf isotopic geochemistry and Paleozoic tectonic implications. Lithos 106, 323–335.
Jiang, C., Yang, J., Feng, B., Zhu, Z., Zhao, M., Chai, Y., Shi, X., Wang, H., Hu, J., 1992. Opening-closing tectonics of Kunlun Mountains. Beijing, Geological Publishing House. 224 (In Chinese with English abstract.
Johnson, J.E., Webb, S.M., Thomas, K., Ono, S., Kirschvink, J.L., Fischer, W.W., 2013. Manganese-oxidizing photosynthesis before the rise of cyanobacteria. Proc. Natl. Acad. Sci. u. s. a. 110, 11238–11243.
Johnson, J.E., Webb, S.M., Ma, C., Fischer, W.W., 2016. Manganese mineralogy and diagenesis in the sedimentary rock record. Geochim. Cosmochim. Acta 173, 210–231.
Kang, L., Xiao, P.X., Gao, X.F., Wang, C., Yang, Z.C., Xi, R.G., 2015. Geochemical characteristics, petrogenesis and tectonic setting of oceanic plagiogranites belt in the northwestern margin of western Kunlun. Acta Petrol. Sin. 31, 2566–2582. In Chinese with English abstract.
Kuleshov, V.N., 2011. Manganese deposits: Communication 2. Major epochs and phases of manganese accumulation in the Earth's history. Lithol. Miner. Resour. 46, 546.
Kuleshov, V., 2017. Isotope Geochemistry: The origin and formation of manganese rocks and ores. Elsevier.
Kuleshov, V.N., Bychkov, A.Y., Nikolaeva, I.Y., Tarnopolskaya, M.E., 2023. Rare earth elements (REE) and isotope composition ($\delta^{13}C$ and $\delta^{18}O$) of manganese ores of Chiatura deposit (Georgia): features of ore formation and genesis. Acta Geochim. 42, 779–801.
Kuwahara, Y., Fujinaga, K., Nozaki, T., Ohta, J., Yano, M., Yasukawa, K., Nakamura, K., Kato, Y., 2022. Iron deposition during recovery from Late Devonian oceanic anoxia: Implications of the geochemistry of the Kawame ferromanganese deposit, Nedamo Belt. Northeast Japan. Glob. Planet. Change 216, 103920.
Li, G.W., Fang, A.M., Wu, F.Y., Liu, X.H., Pan, Y.S., Wang, S.G., 2009. Studies on the U-Pb ages and Hf isotopes of zircons in the Aoyitake plagioclase granite, west Tarim. Acta Petrol. Sin. 25, 166–172. In Chinese with English abstract.
Li, D., Yang, S., Chen, H., Cheng, X., Li, K., Jin, X., Li, Z., Li, Y., Zou, S., 2014. Late Carboniferous crustal uplift of the Tarim plate and its constraints on the evolution of the Early Permian Tarim Large Igneous Province. Lithos 204, 36–46.
Li, D., Fu, Y., Liu, Q., Reinfelder, J.R., Hollings, P., Sun, X., Tan, C., Dong, Y., Ma, W., 2020. High-resolution LA-ICP-MS mapping of deep-sea polymetallic micronodules and its implications on element mobility. Gondwana Res. 81, 461–474.
Li, R.S., Ji, W.H., Chen, S., Wang, X., 2011. Paleozoic tectonic lithofacies paleogeography map of the Qinghai-Tibet Plateau and its adjacent areas. Geological Publishing House (In Chinese).
Li, W.J., Peng, Z.-D., Dong, Z.G., Zhang, B.L., Gao, B.Y., Zhang, L.C., Zhu, M.-T., Robbins, L.J., Konhauser, K.O., 2022a. Direct Re-Os dating of manganese carbonate ores and implications for the formation of the Ortokarnash manganese deposit, Northwest China. Econ. Geol. 117, 237–252.
Li, S.L., Sha, J.H., Yan, J.J., Pei, Q.M., 2018. Accessing the supply risk for manganese resources in China under two-dimensional coordinate system. China Min. Mag. 27, 15–19. In Chinese with English abstract.
Li, X.Y., Wang, E.J., Wu, C.Q., Zhao, D.H., Hua, B., Zhang, Z.W., Xu, J.H., Jin, Z.R., 2022b. The redox-conditions controlled manganese carbonate mineralization in the Late Paleozoic Qiaerlong deep basin, Western Kunlun Mountains. China. Ore Geol. Rev. 147, 104993.
Liao, S., Jiang, Y.H., Jiang, S.Y., Yang, W.Z., Zhou, Q., Jin, G.D., Zhao, P., 2010. Subducting sediment-derived arc granitoids: evidence from the Datong pluton and its quenched enclaves in the western Kunlun orogen, northwest China. Mineral. Petrol. 100, 55–74.
Liu, Y., Chou, I.M., Chen, J., Wu, N., Li, W., Bagas, L., Ren, M., Liu, Z., Mei, S., Wang, L., 2023b. Oldhamite: A new link in upper mantle for C-O-S-Ca cycles and an indicator for planetary habitability. Natl. Sci. Rev. 10, nwad159.

Liu, C., Jarochowska, E., Du, Y., Vachard, D., Munnecke, A., 2017. Stratigraphical and $\delta^{13}C$ records of Permo-Carboniferous platform carbonates, South China: responses to late Paleozoic icehouse climate and icehouse–greenhouse transition. Palaeogeogr., Palaeoclimatol. Palaeoecol. 474, 113–129.
Liu, Z., Jiang, Y.H., Jia, R.Y., Zhao, P., Zhou, Q., Wang, G.C., Ni, C.-Y., 2014. Origin of Middle Cambrian and Late Silurian potassic granitoids from the western Kunlun orogen, northwest China: a magmatic response to the Proto-Tethys evolution. Mineral. Petrol. 108, 91–110.
Liu, X., Wang, Q., Peng, Y., Yin, R., Ma, Y., Zhao, L., Zhang, S., 2023a. Intensified and apace bauxitization over the paleo-karstic surface linked to volcanism. Geol. Soc. Am. Bull. 135, 1187–1205.
Ludwig, K.R., 2003. User's manual for Isoplot 3.00: a geochronological toolkit for Microsoft Excel. Kenneth R. Ludwig.
Ma, Z., Liu, X., Yu, W., Du, Y., Du, Q., 2019. Redox conditions and manganese metallogenesis in the Cryogenian Nanhua Basin: Insight from the basal Datangpo Formation of South China. Palaeogeogr., Palaeoclimatol. Palaeoecol. 529, 39–52.
Marshall, J., 1998. Cathodoluminescence of geological materials. Wiley Online Library, p. 146.
Matte, P., Tapponnier, P., Arnaud, N., Bourjot, L., Avouac, J.P., Vidal, P., Qing, L., Yusheng, P., Yi, W., 1996. Tectonics of Western Tibet, between the Tarim and the Indus. Earth Planet. Sci. Lett. 142, 311–330.
Mattern, F., Schneider, W., 2000. Suturing of the Proto- and Paleo-Tethys oceans in the western Kunlun (Xinjiang, China). J. Asian Earth Sci. 18, 637–650.
Maynard, J.B., 2010. The Chemistry of Manganese Ores through Time: A Signal of Increasing Diversity of Earth-Surface Environments. Econ. Geol. 105, 535–552.
Maynard, J.B., 2014. 9.11 - Manganiferous Sediments, Rocks, and Ores. In: Holland, H.D., Turekian, K.K. (Eds.), Treatise on Geochemistry (second Edition). Elsevier, Oxford, pp. 327–349.
McLennan, S.M., 1989. Rare earth elements in sedimentary rocks: Influence of provenance and sedimentary processes. Rev. Mineral. 21, 169–200.
Morad, S., Al-Aasm, I.S., 1997. Conditions of rhodochrosite-nodule formation in Neogene-Pleistocene deep-sea sediments: evidence from O, C and Sr isotopes. Sediment. Geol. 114, 295–304.
Nakagawa, M., Santosh, M., Maruyama, S., 2009. Distribution and mineral assemblages of bedded manganese deposits in Shikoku, Southwest Japan: Implications for accretion tectonics. Gondwana Res. 16, 609–621.
Nealson, K.H., Tebo, B.M., Rosson, R.A., 1988. Occurrence and Mechanisms of Microbial Oxidation of Manganese. In: Laskin, A.I. (Ed.), Advances in Applied Microbiology. Academic Press, pp. 279–318.
Pan, Y.S., Fang, A.M., 2010. Formation and evolution of the Tethys in the Tibetan Plateau. Sci. Geol. Sin. 45, 92–101. In Chinese with English abstract.
Pattan, J.N., Parthiban, G., 2011. Geochemistry of ferromanganese nodule–sediment pairs from Central Indian Ocean Basin. J. Asian Earth Sci. 40, 569–580.
Pelleter, E., Fouquet, Y., Etoubleau, J., Cheron, S., Labanieh, S., Josso, P., Bollinger, C., Langlade, J., 2017. Ni-Cu-Co-rich hydrothermal manganese mineralization in the Wallis and Futuna back-arc environment (SW Pacific). Ore Geol. Rev. 87, 126–146.
Peng, Z.X., 1991. The genetic relationship between the ratio of Co/Ni and manganese ore. Geol. Explor., 16–17 In Chinese with English abstract.
Peters, K.E., Moldowan, J.M., 1993. The biomarker guide: interpreting molecular fossils in petroleum and ancient sediments. Prentice Hall Inc., New Jersey, pp. 111–210.
Polgári, M., Gyollai, I., 2022. Comparative study of formation conditions of Fe-Mn ore microbialites based on mineral assemblages: A critical self-overview. Minerals. 12, 1273.
Polgári, M., Németh, T., Pál-Molnár, E., Futó, I., Vigh, T., Mojzsis, S.J., 2016. Correlated chemostratigraphy of Mn-carbonate microbialites (Úrkút, Hungary). Gondwana Res. 29, 278–289.
Polgári, M., Gyollai, I., Fintor, K., Horváth, H., Pál-Molnár, E., Biondi, J.C., 2019. Microbially mediated ore-forming processes and cell mineralization. Front. Microbiol. 10, 489777.
Qin, Y.K., Zhang, H.C., Yao, J.Q., 2010. Geochemical Characteristics and Geological Impl ication of the Xialei Manganese Depost, Daxin County. Guangxi. Geol. Rev. 56, 664–672. In Chinese with English abstract.
Reisberg, L., Meisel, T., 2002. The Re-Os isotopic system: A review of analytical techniques. Geostand. Newsl. 26, 249–267.
Renard, M., Rafelis, M.d., Emmanuel, L., Moullade, M., Masse, J.P., Kuhnt, W., Bergen, J.A., Tronchetti, G., 2005. Early Aptian $\delta^{13}C$ and manganese anomalies from the historical Cassis-La Bédoule stratotype sections (S.E. France): relationship with a methane hydrate dissociation event and stratigraphic implications., Notebooks on Geology, Brest, CG2005_A2004.
Roy, S., 2006. Sedimentary manganese metallogenesis in response to the evolution of the Earth system. Earth-Sci. Rev. 77, 273–305.
Rubinstein, N.A., Zappettini, E.O., 2015. Origin and age of rift related fluorite and manganese deposits from the San Rafael Massif. Argentina. Ore Geol. Rev. 66, 334–343.
Schier, K., Bau, M., Smith, A.J.B., Beukes, N.J., Coetzee, L.L., Viehmann, S., 2020. Chemical evolution of seawater in the Transvaal Ocean between 2426 Ma (Ongeluk Large Igneous Province) and 2413 Ma ago (Kalahari Manganese Field). Gondwana Res. 88, 373–388.
Shanmugam, G., 1985. Significance of coniferous rain forests and related organic matter in generating commercial quantities of oil, Gippsland Basin, Australia. Am. Assoc. Pet. Geol. Bull. 69, 1241–1254.
She, J., Zhu, Z., Jia, J., Duan, X., Peng, G., Di, X., 2020. Distribution and characteristics of major faults in Xinjiang. Xinjiang Geol. 38, 9–20. In Chinese with English abstract.
Sun, J., Dong, Y., Ma, L., Chen, S., Jiang, W., 2022. Devonian to Triassic tectonic evolution and basin transition in the East Kunlun-Qaidam area, northern Tibetan Plateau: Constraints from stratigraphy and detrital zircon U-Pb geochronology. Geol. Soc. Am. Bull. 134, 1967–1993.
Tebo, B.M., Bargar, J.R., Clement, B.G., Dick, G.J., Murray, K.J., Parker, D., Verity, R., Webb, S.M., 2004. Biogenic manganese oxides: properties and mechanisms of formation. Annu. Rev. Earth Planet. Sci. 32, 287–328.
Thamdrup, B., 2000. Bacterial Manganese and Iron Reduction in Aquatic Sediments. In: Schink, B. (Ed.), Advances in Microbial Ecology. Springer, US, Boston, MA, pp. 41–84.
Toth, J.R., 1980. Deposition of submarine crusts rich in manganese and iron. Geol. Soc. Am. Bull. 91, 44–54.
Veglio, F., Toro, L., 1994. Fractional factorial experiments in the development of manganese dioxide leaching by sucrose in sulphuric acid solutions. Hydrometallurgy 36, 215–230.
Wang, Z.H., 2004. Tectonic evolution of the western Kunlun orogenic belt, western China. J. Asian Earth Sci. 24, 153–161.
Wang, Q., Deng, J., Liu, X., Zhao, R., Cai, S., 2016. Provenance of Late Carboniferous bauxite deposits in the North China Craton: New constraints on marginal arc construction and accretion processes. Gondwana Res. 38, 86–98.
Wang, X., Li, Y., Li, Y.Z., Liu, Y.W., Duan, J.S., Ding, H.R., Wang, C.Q., Lu, A.H., 2018. Effects of Mg^{2+} and SO_4^{2-} on Mn-carbonate mineralization Induced by microorganisms in shallow seas. Earth Sci. 43, 145–156. In Chinese with English abstract.
Wang, P., Zhao, G., Han, Y., Liu, Q., Yao, J., Yu, S., Li, J., 2020. Timing of the final closure of the Proto-Tethys Ocean: Constraints from provenance of early Paleozoic sedimentary rocks in West Kunlun. NW China. Gondwana Res. 84, 151–162.
Webb, S.M., Tebo, B.M., Barger, J.R., 2005. Structural Influences of Sodium and Calcium Ions on the Biogenic Manganese Oxides Produced by the Marine Bacillus Sp., Strain SG-1. Geomicrobiol. J. 22, 181–193.
West, D.P., Yates, M.G., Gerbi, C., Barnard, N.Q., 2008. Metamorphosed Ordovician Fe-and Mn-rich rocks in south-central Maine: From peri-Gondwanan deposition through Acadian metamorphism. Am. Mineral. 93, 270–282.
Wu, L., Jin, Z., Chu, Z., Liu, K., 2021. Re-Os isotopic dating procedures for organic-rich samples. Pet. Geol. Exp. 43, 513–523. In Chinese with English abstract.
Xia, Y., Sui, Q., He, Y., Ji, W., Chen, D., Zhao, X., Zhao, M., Gao, X., Wang, K., Zhang, L., 2023. Carboniferous back-arc bimodal rocks in West Kunlun during northward subduction of the Paleo-Tethys. Int. Geol. Rev. 1–19. https://doi.org/10.1080/00206814.2023.2233016.
Xiao, J., He, J., Yang, H., Wu, C., 2017. Comparison between Datangpo-type manganese ores and modern marine ferromanganese oxyhydroxide precipitates based on rare earth elements. Ore Geol. Rev. 89, 290–308.
Xiao, W.J., Windley, B.F., Chen, H.L., Zhang, G.C., Li, J.L., 2002. Carboniferous-Triassic subduction and accretion in the western Kunlun, China: Implications for the collisional and accretionary tectonics of the northern Tibetan Plateau. Geology 30, 295–298.
Xiao, W.J., Windley, B.F., Liu, D.Y., Jian, P., Liu, C.Z., Yuan, C., Sun, M., 2005. Accretionary Tectonics of the Western Kunlun Orogen, China: A Paleozoic-Early Mesozoic, Long-Lived Active Continental Margin with Implications for the Growth of Southern Eurasia. J. Geol. 113, 687–705.
Xie, J.C., Du, J.G., Xu, W., Yang, X.Y., 2006. The geological and geochemical characteristics of manganese-bearing sequences of Guichi, Anhui Province. East China. Geol. Rev., 396–408 In Chinese with English abstract.
Xu, H., Gao, J., Yang, R., Feng, K., Wang, L., Chen, J., 2021. Metallogenic mechanism of large manganese deposits from Permian manganese ore belt in western South China Block: New mineralogical and geochemical evidence. Ore Geol. Rev. 132, 103993.
Yan, H., Pi, D., Xu, L., Sun, K., 2023. The Perturbation of the Guadalupian Marine Environment Triggered by Early-Stage Eruption of the Emeishan Large Igneous Province: Rare Earth Element and Sr-Nd Isotope Evidence from Zunyi Manganese Deposit. South China. Miner. 13, 965.
Yang, R.D., Gao, J.P., Cheng, M.L., Wei, H.R., Xu, L.Q., Feng, W.X., Wei, X., 2010. Sedimentary geochemistry of manganese deposit of the Neoproterozoic Datangpo Formation in Guizhou Province. China. Acta Geol. Sin. 84, 1781–1790. In Chinese with English abstract.
Yang, C., Xu, H., Yin, R., Wang, L., Wu, C., Grasby, S.E., Gao, J., 2023. The Zunyi manganese deposit, South China: A consequence of climatic-oceanic changes triggered by the eruption of Emeishan Large Igneous Province? Ore Geol. Rev. 158, 105530.
Yao, Y.C., Qiu, X., Wang, H.M., Duan, Y., 2018. Dolomite Formation Mediated by Halophilic Archaeal Cells under Different Conditions and Carboxylated Microspheres. Earth Sci. 43, 449–458. In Chinese with English abstract.
Yin, J.N., Xiao, K.Y., 2014. Resources potential analysis and metallogenic prospect of Mn resources in China. Geol. China 41, 1424–1437. In Chinese with English abstract.
Yu, W.C., Algeo, T.J., Du, Y.S., Maynard, B., Guo, H., Zhou, Q., Peng, T.P., Wang, P., Yuan, L.J., 2016. Genesis of Cryogenian Datangpo manganese deposit: Hydrothermal influence and episodic post-glacial ventilation of Nanhua Basin, South China. Palaeogeogr. Palaeoclimatol. Palaeoecol. 459, 321–337.

Yun, J., 2015. Petrogenesis and the tectonic setting of the Lower Paleozoic volcanic rocks in the Northern Belt of West Kunlun. China University of Geosciences (Beijing). (In Chinese with English abstract). Master's thesis.
Yun, J., Gao, X.F., Xiao, P.X., Kang, L., Li, P., 2015. Geochemical characteristics of the Lower Carboniferous volcanic rocks of the Wuluate Formation in the Western Kunlun Mountains and their geological significance. Geol. China 42, 587–600. In Chinese with English abstract.
Zhang, Y., Gong, W., Shan, X., Wang, C., 2022. Extension in the West Kunlun Mountains, NW Tibet: Insights from seismicity and analytical modeling. Tectonophysics 839, 229526.
Zhang, B.L., Wang, C.L., Robbins, L.J., Chang, Z.L., Konhauser, K.O., Dong, Z.G., Li, W.J., Peng, Z.D., Zheng, M.T., 2020. Petrography and Geochemistry of the Carboniferous Ortokarnash Manganese Deposit in the Western Kunlun Mountains, Xinjiang Province, China: Implications for the Depositional Environment and the Origin of Mineralization. Econ. Geol. 115, 1559–1588.
Zhang, C., Yu, H., Ye, H., Zhao, Y., Zhang, D., 2006. Aoyitake plagiogranite in western Tarim Block, NW China: Age, geochemistry, petrogenesis and its tectonic implications. Sci. China. Ser. d: Earth Sci. 49, 1121–1134.
Zhang, D., Zhang, Z., Santosh, M., Cheng, Z., He, H., Kang, J., 2013. Perovskite and baddeleyite from kimberlitic intrusions in the Tarim large igneous province signal the onset of an end-Carboniferous mantle plume. Earth Planet. Sci. Lett. 361, 238–248.
Zhang, Y.X., Zhang, K.J., 2017. Early Permian Qiangtang flood basalts, northern Tibet, China: A mantle plume that disintegrated northern Gondwana? Gondwana Res. 44, 96–108.
Zhang, C.L., Zou, H.-B., Ye, X.-T., Chen, X.Y., 2019. Tectonic evolution of the West Kunlun Orogenic Belt along the northern margin of the Tibetan Plateau: Implications for the assembly of the Tarim terrane to Gondwana. Geosci. Front. 10, 973–988.
Zhou, Q., Du, Y.S., Yuan, L.J., Zhang, S., Yu, W.C., Yang, S.T., Liu, Y., 2016. The Structure of the Wuling Rift Basin and Its Control on the Manganese Deposit during the Nanhua Period in Guizhou-Hunan-Chongqing Border Area. South China. Earth Sci. 41, 177–188. In Chinese with English abstract.
Zhu, R., Luo, P., Luo, Z., 2002. Lithofacies palaeogeography of the late Devonian and Carboniferous in Tarim Basin. J. Palaeogeogr. 4, 13–24. In Chinese with English abstract.